ANKARA YILDIRIM BEYAZIT UNIVERSITY

GRADUATE SCHOOL OF NATURAL AND APPLIED SCIENCE



STUDY OF UTILIZING MULTIPLE INERTIAL MEASUREMENT UNITS FOR STRAPDOWN INERTIAL NAVIGATION SYTEMS WITHOUT GLOBAL POSITIONING SYSTEM AID

M.Sc. Thesis by

Osman TOKLUOĞLU

Department of Electrical and Electronics Engineering

June 2019

ANKARA

STUDY OF UTILIZING MULTIPLE INERTIAL MEASUREMENT UNITS FOR STRAPDOWN INERTIAL NAVIGATION SYSTEMS WITHOUT GLOBAL POSITIONING SYSTEM AID

A Thesis Submitted to

The Graduate School of Natural and Applied Sciences of

Ankara Yıldırım Beyazıt University

In partial Fulfillment of the Requirements for the Degree of Master of Science in Electrical and Electronics Engineering, Department of Electrical and Electronics Engineering

by

Osman TOKLUOĞLU

June, 2019

ANKARA

M.Sc. THESIS EXAMINATION RESULT FORM

We have read the thesis entitled **"STUDY OF UTILIZING MULTIPLE INERTIAL MEASUREMENT UNITS FOR STRAPDOWN INERTIAL NAVIGATION SYTEMS WITHOUT GLOBAL POSITIONING SYSTEM AID"** under the supervision of **ASSOC. PROF. DR. ENVER ÇAVUŞ** and we certify that in our opinion it is fully adequate, in scope and in quality, as a thesis for the degree of Master of Science.

Assoc. Prof. Dr. Enver ÇAVUŞ

Supervisor

Prof. Dr. Alaa El-Rouby

Jury Member

Assist. Prof. Dr. Mehmet Efe ÖZBEK

Jury Member

Prof. Dr. Ergün ERASLAN

Director

Graduate School of Natural and Applied Science

ETHICAL DECLARATION

I hereby declare that in this thesis which has been prepared in accordance with the Thesis Writing Manual of Graduate School of Natural and Applied Sciences,

- All data, information and documents are obtained in the framework of academic and ethical rules,
- All information, documents and assessments are presented in accordance with scientific ethics and morals,
- All the materials that have been utilized are fully cited and referenced,
- No change has been made on the utilized materials,
- All the works presented are original,

and in any contrary case of above statements, I accept to renounce all my legal rights.

Date: 20/05/2019

Signature:

Name & Surname: Osman TOKLUOĞLU

ACKNOWLEDGMENTS

First of all, I would like to express my sincere gratitude to my supervisor, Assoc. Prof. Dr. Enver ÇAVUŞ for his support and motivation during my study. He always helped me whenever I ran into a trouble spot or had a question about my research or writing.

Secondly, I would like to express my appreciation to Prof. Dr. Alaa EL-ROUBY and Assist. Prof. Dr. Mehmet Efe ÖZBEK for their help and support.

Finally, I would like to thank my family for their life long support.

2019, 20 May **Osman TOKLUOĞLU**

STUDY OF UTILIZING MULTIPLE INERTIAL MEASUREMENT UNITS FOR STRAPDOWN INERTIAL NAVIGATION SYSTEMS WITHOUT GLOBAL POSITIONING SYSTEM AID

ABSTRACT

Due to their small sizes and light weights micro electromechanical systems inertial measurement units have become popular in inertial navigation systems. Although, when the data taken from micro electromechanical systems inertial measurement units are fused with the global positioning system data it is most likely to obtain a precise result, in regions where global positioning system data is not available results may be misleading. This article studies the error profile of an inertial navigation system in an environment where there is a lack of global positioning system data utilizing multiple inertial measurement units. Using a simulation framework, tracking performance of an inertial navigation system employing single inertial measurement unit is compared with a triple inertial measurement unit inertial navigation system. The simulation results reveal that utilizing extra inertial measurement units in an environment where there is a lack of global positioning system data improves the error profile where up to 82%, 85%, and 83% reductions in latitude, longitude and altitude error figures respectively.

Keywords: Inertial navigation system, micro electromechanical systems inertial measurement units, global positioning system, multiple inertial measurement unit inertial navigation system, unmanned aerial vehicle navigation

KÜRESEL KONUMLAMA SİSTEMİ YARDIMININ OLMADIĞI BÖLGELERDE ATALETSEL SEYRÜSEFER SİSTEMLERİNDE ÇOKLU ATALET ÖLÇÜM BİRİMİ KULLANMA ÇALIŞMASI

ÖZ

Küçük boyutları ve hafiflikleri nedeniyle mikro elektromekanik sistem teknolojisi ile üretilen atalet ölçüm birimleri, ataletsel seyrüsefer sistemlerinde popüler hale gelmiştir. Her ne kadar mikro elektromekanik sistem teknolojisi ile üretilen atalet ölçüm birimlerinden alınan veriler küresel konumlandırma sistemi verileriyle birlikte kullanıldıklarında tutarlı sonuçlar elde edilse de küresel konumlandırma sistemi verilerinin bulunmadığı bölgelerde elde edilen sonuçlar hatalı olmaktadır. Bu makale, çoklu atalet ölçüm birimi kullanan bir ataletsel seyrüsefer sisteminin küresel konumlandırma sistemi verilerinin olmadığı bir ortamda hata profilini incelemektedir. Tek bir atalet ölçüm birimi kullanan farklı ataletsel seyrüsefer sistemlerinin performansları ile üç adet atalet ölçüm birimi kullanan bir ataletsel seyrüsefer sisteminin performansı bir simülasyon ortamı yardımı ile karşılaştırılmıştır. Simülasyon sonuçları, küresel konumlandırma sistemi verilerinin olmadığı bir ortamda çoklu atalet ölçüm birimlerinin kullanılmasının, sırasıyla enlem, boylam ve yükseklik hata rakamlarında % 82, % 85 ve % 83 düşüşlere neden olarak ataletsel seyrüsefer sistemin performansının artmasını sağladığını göstermektedir.

Anahtar Kelimeler: Ataletsel seyrüsefer sistemi, mikro elektromekanik sistemler atalet ölçüm birimleri, küresel konumlandırma sistemi, çoklu atalet ölçüm ünitesi atalet seyrüsefer sistemi, insansız hava aracı navigasyonu

CONTENTS

M.Sc. THESIS EXAMINATION RESULT FORM……..……..ii

ETHICAL DECLARATION……..……..iii

ACKNOWLEDGEMENTS…….……iv

ABSTRACT……..……v

ÖZ…….……..…vi

CONTENTS……..…vi

LIST OF SYMBOLS……..…ix

LIST OF TABLES……...xiv

LIST OF FIGURES……..xv

CHAPTER 1 - INTRODUCTION

1.1 Introduction….....1

CHAPTER 2 - BASIC PRINCIPLES OF SINS

2.1 Inertial Measurement Unit (IMU).....5

2.1.1 MEMS Inertial Measurement Unit (MEMS IMU) 5

2.1.2 Gyroscope.....7

2.1.3 Accelerometer.....14

2.2 Fundamental Principles of INS.....19

2.2.1 Reference Frames.....19

2.2.2 Direction Cosine Matrix (DCM).....23

2.2.3 Inertial Navigation System Mechanism.....25

CHAPTER 3 - METHODS USED FOR THE NAVIGATION IN GPS-DENIED ENVIRONMENTS.....30
3.1 Simultaneous Localization and Mapping (SLAM).....30
3.2 Visual Odometry (VO).....33
3.3 Utilizing Multiple Inertial Sensors and Multiple IMUs.....36
CHAPTER 4 - COMPARATIVE STUDY OF SINGLE AND MULTIPLE IMU SINS IN A SIMULATION ENVIRONMENT.....42
4.1 Methodology.....42
4.1.1 Simulation Framework.....43
4.2 Single and Multiple IMU SINS Comparison.....46
4.2.1 Reference Trajectory Selection.....48
4.2.2 IMU Selection.....48
4.2.3 GPS-denied Region Model.....50
4.2.4 Simulation Results.....50
CHAPTER 5 - CONCLUSIONS, PERSPECTIVES AND FUTURE WORKS.....54
REFERENCES.....56
CURRICULUM VITAE.....61

NOMANCLATURE

Roman Letter Symbols

A	Area enclosed by the light beams
a	Acceleration
a^b	Acceleration data expressed in body axis
a^n	True acceleration vectors expressed in navigation frame
b_g	Static bias for gyroscopes
C_b^i	Direction cosine matrix used to convert the data from body frame to inertial frame
$\dot{C}_b^i$	Time derivative of C_b^i
C_n^b	Direction cosine matrix used to convert the data from navigation frame to body frame
dt	Time difference
e	True attitude vector
F_{C_z}	Coriolis force
F_{Drive}	Drive force
f	Acceleration occurred due to the forces other than gravity
f^b	Accelerometer data expressed in body frame axis
f^i	Accelerometer data expressed in inertial frame axis
f_{xb}	Accelerometer data expressed in body axis with respect to x axis
f_{zb}	Accelerometer data expressed in body axis with respect to z axis
f_{xi}	Accelerometer data expressed in inertial frame axis with respect to x axis
f_{zi}	Accelerometer data expressed in inertial frame axis with respect to z axis
f_{noise}^b	Noisy accelerometer output data

f_{cor}^{n}	Coriolis force expressed in navigation axis
m	Mass
N	Number of fiber turns
p	True position vector
p_G^n	Position data coming from GPS
S	Skew symmetric form of v^n
T	True input data
t_s	Simulation time vector
x_b	Body frame *x* axis
x_e	Earth frame *x* axis
x_i	Inertial frame *x* axis
$\dot{x}_i$	Time derivative of the distance along *x* axis expressed in inertial frame
$x_{(-)}$	State vector belonging the previous time period
y_b	Body frame *y* axis
y_e	Earth frame *y* axis
y_i	Inertial frame *y* axis
$\ddot{y}$	Second derivative of the distance taken along y axis with respect to time
z_b	Body frame *z* axis
z_e	Earth frame *z* axis
z_i	Inertial frame *z* axis
$\dot{z}$	First derivative of the distance taken along z axis with respect to time
$\dot{z}_i$	Time derivative of the distance along *z* axis expressed in inertial frame
v	Velocity
v_{xi}	Velocity data expressed in inertial frame axis with respect to x axis

v_{zi}	Velocity data expressed in inertial frame axis with respect to z axis
$\dot{v}_{xi}$	Time derivative of the velocity data expressed in inertial frame axis with respect to x axis
$\dot{v}_{zi}$	Time derivative of the velocity data expressed in inertial frame axis with respect to z axis
v^n	True velocity vectors expressed in navigation frame
v_G^n	Velocity data coming from GPS

Greek Letter Symbols

ω	Angular velocity
$\Delta\varphi$	Phase difference
λ_0	Free space wavelength
Ω	Angular velocity of the system and
ω_{ib}^b	Attitude of the vehicle body frame with respect to the inertial reference frame expressed in body frame
ω_{nb}^b	Attitude of the vehicle body frame with respect to the navigation frame expressed in body frame
ω_{ie}^n	Attitude of the earth frame with respect to the inertial frame expressed in navigation frame
ω_{en}^n	Attitude of the navigation frame with respect to the earth frame expressed in navigation frame
ω_{yb}	Attitude of the vehicle body frame with respect to the y axis
Ω_{ib}^b	Skew symmetric matrix formed by ω_{ib}^b
θ	Overall attitude of a body
$\dot{\theta}$	Time derivative of overall attitude of a body
η_g	WGN element for gyroscopes

δb_g	Dynamic bias for gyroscopes
τ_g	Correlation time
ω_{noise}^{b}	Noisy gyroscope output data
$\eta_{g\delta b}$	Dynamic bias noise for gyroscopes
$\eta_{g\delta b(+)}$	Dynamic bias noise for gyroscopes for next time interval
η_f	WGN element for accelerometers
b_f	Static bias for accelerometers
$\eta_{f\delta b}$	Dynamic bias noise for accelerometers
$\eta_{f\delta b(+)}$	Dynamic bias noise for accelerometers for next time interval
σ	Standard deviation

Acronyms

ARW	Angular Random Walk
DCM	Direction Cosine Matrix
EKF	Extended Kalman Filter
GPS	Global Positioning System
Hz	Hertz
IMU	Inertial Measurement Unit
INS	Inertial Navigation system
KF	Kalman Filter
LO	Laser Odometry
MEMS	Micro Electromechanical Systems
NED	North-East-Down

ROI	Regions of Interest
SEM	Scanning Electron Micrograph
SINS	Strapdown Inertial Navigation System
SLAM	Simultaneous Localization and Mapping
UAV	Unmanned Aerial Vehicle
VO	Visual Odometry
VRW	Velocity Random Walk
WGN	White Gaussian Noise

LIST OF TABLES

Table 4.1 IMU Profiles……49

LIST OF FIGURES

Figure 1.1 INS block diagram……1
Figure 2.1 IMU-L3G4200D with three axis gyros and accelerometers……..6
Figure 2.2 IMU-HW-579 with three axis gyros, accelerometers and magnetometers……6
Figure 2.3 Replica of the gyroscope invented by Leon Foucault……8
Figure 2.4 Schematic diagram of a two-axis gyroscope……8
Figure 2.5 Schematic representation of the Sagnac effect……..9
Figure 2.6 The schematic representation of a fiber optic gyroscope based on the Sagnac effect……10
Figure 2.7 Coriolis force on a moving particle……12
Figure 2.8 Basic MEMS-gyroscope principle……..12
Figure 2.9 SEM of a z-axis vibratory gyroscope with digital output……13
Figure 2.10 Simple mechanical accelerometer……14
Figure 2.11 Force-feedback pendulous accelerometer……15
Figure 2.12 The structure of a tilting mirror fiber optic accelerometer……16
Figure 2.13 The functional schematic of a tilting mirror fiber optic accelerometer……..17
Figure 2.14 MEMS accelerometer structure……18
Figure 2.15 Structure of a 3D MEMS accelerometer……18
Figure 2.16 Electronic circuitry of a 3D MEMS accelerometer……19
Figure 2.17 The inertial frame (i-frame)……...20
Figure 2.18 The earth frame (e-frame)……21
Figure 2.19 The inertial frame, earth frame and navigation frame on the same figure…..22
Figure 2.20 Orthogonal axis of the body frame……23
Figure 2.21 Roll, pitch and yaw axis of the vehicle……..23
Figure 2.22 Two-dimensional SINS……26
Figure 2.23 Two-dimensional navigation motion scenario……..27
Figure 2.24 SINS block diagram……..29
Figure 3.1 Mobile tour guide robot, Minerva……...31
Figure 3.2 Landmark selection for SLAM……32
Figure 3.3 SLAM process schematic for a UAV……..33
Figure 3.4 Block diagram of visual odometry (VO)……34

Figure 3.5 Representation of the visual odometry method……...34

Figure 3.6 An illustration of the VO method……35

Figure 3.7 Block diagram of the combination of IMU and VO data……36

Figure 3.8 Individual gyroscope drifts (left), drift of the virtual gyroscope (right)……...37

Figure 3.9 Block diagram of the proposed multiple gyroscope method in [9]……..38

Figure 3.10 Navigation system containing 100 inertial sensors with two digital signal processors……38

Figure 3.11 Orthogonal configuration (left), skew-redundant configuration (right) for redundant-IMU applications……39

Figure 3.12 The embedded MIMU platform consisting of 18 IMUs……40

Figure 3.13 Multiple IMU system consisting of four MEMS IMUs……40

Figure 4.1 General simulation strategy……43

Figure 4.2 Diagram of SINS, GPS, and EKF integration……..47

Figure 4.3 Trajectory used in this study……48

Figure 4.4 Geographic coordinate system……50

Figure 4.5 Latitude errors of the INSs without GPS aid……51

Figure 4.6 Longitude errors of the INSs without GPS aid……52

Figure 4.7 Altitude errors of the INSs without GPS aid……53

CHAPTER 1

INTRODUCTION

1.1 Introduction

Inertial navigation system (INS) is a self-contained navigation system which consists of an inertial measurement unit (IMU) for angular rotation and acceleration measurement and a processing system for position and velocity estimation. IMUs use gyroscope and accelerometer sensors to measure rotational motion and change in velocity. The processing unit takes the data coming from accelerometers and gyroscopes and give the position and velocity estimation of the moving vehicle by fusing these two data as illustrated in Figure 1.1.

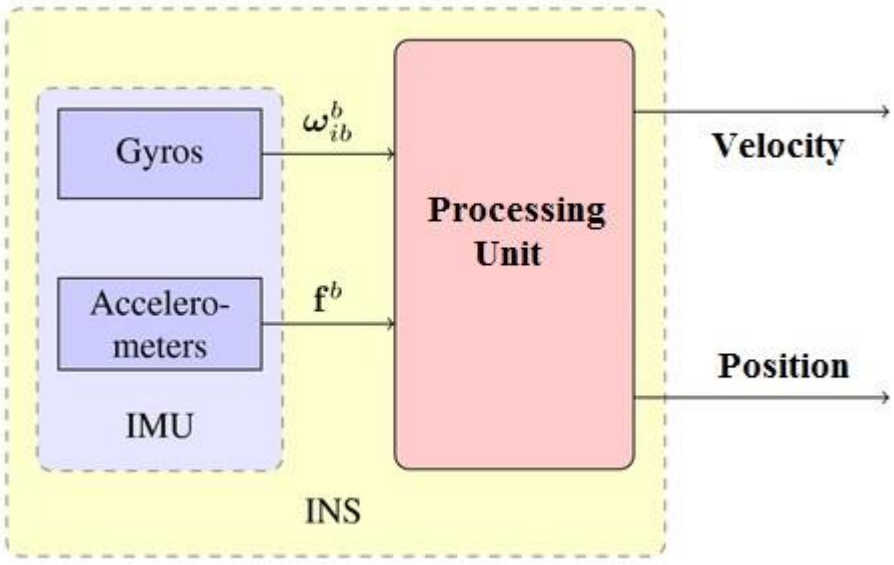


Figure 1.1 Inertial navigation system block diagram

In Figure 1.1, ω_{ib}^{b} represent the angular rotation data coming from the gyroscopes and f^b represents the acceleration force coming from the accelerometers mounted on the inertial

measurement unit. Subscripts and superscripts represent the reference frames which are discussed in detail in Chapter 3.2.1.

Inertial Navigation Systems are generally used with the global positioning system (GPS) aid. In other words, both the data taken from INS and the data coming from GPS signal are combined to determine the location of a mobile target. However, GPS signals are not available all the time as signal blockages occur in some regions due to signal jamming, hostile weather conditions or environmental factors. In literature, such regions are called GPS-denied regions or GPS-denied environments. As navigation without GPS data is commonly encountered in many applications such as military operations or indoor navigations, navigation in GPS-denied regions has become an important topic for researchers to work on.

When GPS signal is unavailable for navigation, the accuracy of the inertial sensors become very critical since in such cases the navigation system solely depends on the accuracy of the data coming from the IMU. Although very high precision mechanical or optical accelerometers and gyroscopes are available, these inertial sensors are generally bulky and expensive. Therefore, for the navigation applications where the cost and size are important such as unmanned aerial vehicle (UAV) or guided missile navigation, micro electromechanical systems (MEMS) gyroscopes and MEMS accelerometers become very attractive [1]. When the data taken from MEMS-IMUs are fused with the GPS signal, the result is most likely to be precise. However, when there is no GPS signal, or the error magnitude of the received GPS signal is high, the INS result may be inaccurate due to the high error profiles of the MEMS IMUs. In addition, as the INS finds the velocity and position of the vehicle by integrating the IMU measurements with respect to time, any errors in the measurement grow over time, further deteriorating the INS estimation. Therefore, it is crucial to minimize the measurement errors of MEMS based IMU systems for an accurate inertial navigation system, especially in GPS denied environments.

In literature, there exist different methods such as simultaneous localization and mapping (SLAM), visual odometry (VO), or different signal processing algorithms [5], [6] to improve the accuracy of the navigation in GPS denied environments. Another common method for high precision navigation in GPS-denied regions is to utilize redundant inertial sensors for acceleration and rotation measurements. For example, in [8], performance of the inertial measurement unit is increased up to 170 times by combining virtually the output data of multiple gyroscopes with a suitable Kalman Filter. In another work, using three gyroscopes with a bias drift of $35^o/h$ hour, the bias error is reduced to $53^o/h$ by virtually combining them [9]. In [10], by combining 100 MEMS inertial sensors for the navigation of an unmanned aerial vehicle in a GPS-denied environment the performance of the system is improved. Similar to utilizing multiple sensors in an inertial measurement unit, employing multiple IMUs that are exactly the same as each other in an INS also appears to be an effective navigation method in a GPS-denied environment. For example, in [11], an embedded IMU platform is designed by using 18 *MPU9150* model IMUs which are 9-axis IMUs for GPS-denied or GPS-degraded region applications. It claims that the standard deviation is reduced by roughly a factor of 3.7. In [12], better inertial navigation performance is achieved with a multiple IMU fusion method by implementing four *MPU9150* model inertial measurement units. It argues that angular random walk (ARW) noise decreases to $0.0022^o/\sqrt{s}$ and velocity random walk (VRW) noise is reduced by %50. In addition, it claims that standard deviation of the combined system is reduced six times in comparison with a single sensor in dynamic tests.

Multiple IMU inertial navigation systems are also used with a GPS aid for more precise navigation performance. For example, in [4], By using MEMS-IMUs oriented in orthogonal and skew-redundant configuration the maximum errors are shown to be reduced up to a factor of 2. In [3], a study about improving accuracy with multiple sensors is conducted and the effect of different configurations of MEMS-IMUs on the error profile is examined for different number of IMUs. It is shown that for systems with large redundancy (i.e. 4 or more IMU triads), the most suitable configuration is the orthogonally

redundant IMU configuration. The important point is that in [3] and [4] inertial navigation systems are aided with GPS.

All the studies mentioned above show that utilizing multiple inertial sensors in an inertial measurement unit or employing multiple inertial measurement units in an inertial navigation system is a prominent method to reduce the error profile of the inertial navigation. However, in [8], [9], [10] emphasis is put on the combination of inertial sensors rather utilization of multiple IMUs. In [3], [4] multiple IMU systems are employed with a GPS aid rather than testing them in a GPS-denied region. In [11], [12] same type of IMUs, *MPU9150,* are used to design a multiple IMU navigation system. In this thesis, the positive effect of using three different type of IMUs as a multiple IMU INS on the error profile of the navigation system in a GPS-denied environment is examined by using NaveGo, a simulation framework for low-cost integrated navigation system [2]. Although there are different types of data fusion algorithms for multiple inertial measurement [7], in this study, without dealing with the performances of these algorithms, the positive effect of using multiple IMUs on the error profile of the navigation system in a GPS-denied environment is examined. The simulation results reveal that utilizing extra IMUs in a GPS denied environment improves the error profile, where up to 82%, 85%, and 83% reductions are obtained in latitude, longitude and altitude error figures respectively.

CHAPTER 2

BASIC PRINCIPLES OF INERTIAL NAVIGATION SYSTEMS

Fundamentally there are two different categories for inertial navigation systems: gimbaled or stabilized platform systems, and strapdown systems. Differences between these two inertial navigation systems are explained in the following sections. In this work strapdown inertial navigation systems are studied as it is more suitable for unmanned aerial vehicles (UAVs).

The organization of Chapter 2 is as follows. In Chapter 2, basic principles of strapdown inertial navigation systems (SINSs) are reviewed. First, a discussion on the IMU and its operation is given in Chapter 2.1, then basic terminologies and useful concepts for a better understanding of the inertial navigation system are explained briefly in Chapter 2.2.

2.1 Inertial Measurement Unit

In Chapter 2.1.1 MEMS IMUs are examined briefly, as they are the most popular inertial measurement units used in UAV navigation systems. Further, for better understanding of the working principle of the inertial measurement units, brief information regarding the types and the basic operation principles of gyroscopes and accelerometers are given in Chapters 2.1.2 and 2.1.3.

2.1.1 MEMS Inertial Measurement Unit (MEMS IMU)

MEMS inertial measurement unit, one of the most important parts in a SINS, is an electronic device where 3 axis gyroscopes and 3 axis accelerometers are used to measure rotational motion and change in velocity respectively in three different axes namely **x**, **y** and **z**. SINS can be defined as an inertial navigation system mounted on a mobile vehicle.

With the developing MEMS technology, it has become possible to produce IMUs having small sizes and lightweights. This facilitated the use of these IMUs in UAVs.

For example, the inertial measurement unit module in Figure 2.1, namely IMU-L3G4200D, whose dimensions are **2 cm x 4 cm** contains 3 MEMS gyroscopes and 3 MEMS accelerometers sensitive in **x, y** and **z** axis [13].



Figure 2.1 IMU-L3G4200D with three axis gyros and accelerometers [13]

It is also possible to add other features to IMUs like measuring the gravitational forces with the help of MEMS magnetometers. Apart from gyros and accelerometers, 3 MEMS magnetometers are mounted in **x, y** and **z** axis on the inertial measurement unit module in Figure 2.2, namely IMU-HW-579 [56].



Figure 2.2 IMU-HW-579 with three axis gyros, accelerometers and magnetometers [56]

In addition to magnetometers, thermometer and barometer can also be added to IMUs. However, it is possible to say that accelerometers and gyroscopes are key components of inertial measurement units. Furthermore, in order to comprehend the operation of IMUs it is of utmost importance to understand the operation principles of accelerometers and gyroscopes. Therefore, brief information regarding the types and the basic operation principles of gyroscopes and accelerometers are given in Chapter 2.1.2 and Chapter 2.1.3.

2.1.2 Gyroscope

The expression *Gyroscope* was first used in the middle of the 19th century [15]. Gyroscope, in general, is a device that is used to detect the deviation of an object from a navigation frame. There are basically three types of gyroscopes which are namely mechanical gyroscopes, optical gyroscopes and micro-electro-mechanical gyroscopes (MEMS-gyros) [14]. Although there are other types of gyroscopes as well, the aforementioned gyroscopes are the most commonly used ones, and they are briefly explained in the following.

2.1.2.1 Mechanical Gyroscopes

Mechanical gyroscopes were first invented by Leon Foucault, a French physicist, in 19th century [16], [17]. The replica of the first gyro designed by Foucault is shown in Figure 2.3.

Mechanical gyros consist of a spinning circular wheel rotating around its axis. When the disc is rotating around its axis, it does not change its direction because of the conservation of the angular momentum.



Figure 2.3 Replica of the gyroscope invented by Leon Foucault [53]

In mechanical gyros, this rotating disc is mounted on gimbals. Although the gimbals change their orientation, the rotating wheel does not change its direction due to the angular momentum conservation. Therefore, there occurs a difference in angle between the gimbals orientation and the spin axis of the rotating wheel. This angle difference used to detect the deviation of the vehicle. Figure 2.4 shows the diagram of a rotating wheel mounted on two gimbals which is called two-axis gyroscope.

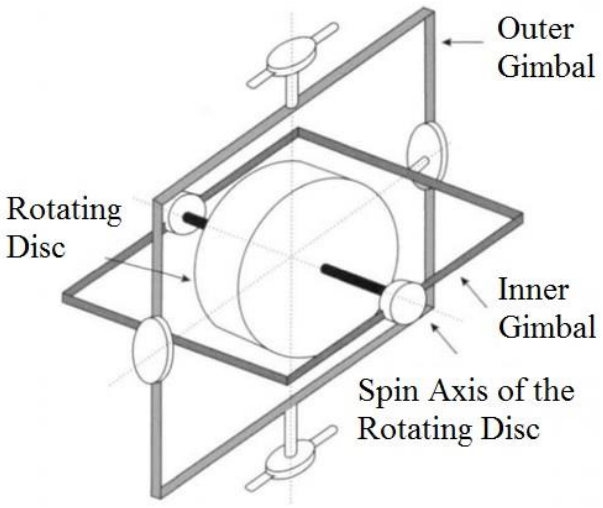


Figure 2.4 Schematic diagram of a two-axis gyroscope [18]

2.1.2.2 Optical Gyroscopes

Gyroscopes sensing the rotation with the help of Sagnac Effect are called optical gyroscopes. The Sagnac Effect was first discovered by Georges Sagnac, in 1913 and this theory has been awarded with his name [19]. Sagnac realized that two light beams moving in opposite directions crossed the same path for different periods while on a rotating disc. Figure 2.5, shows the basic experimental setup of Sagnac.

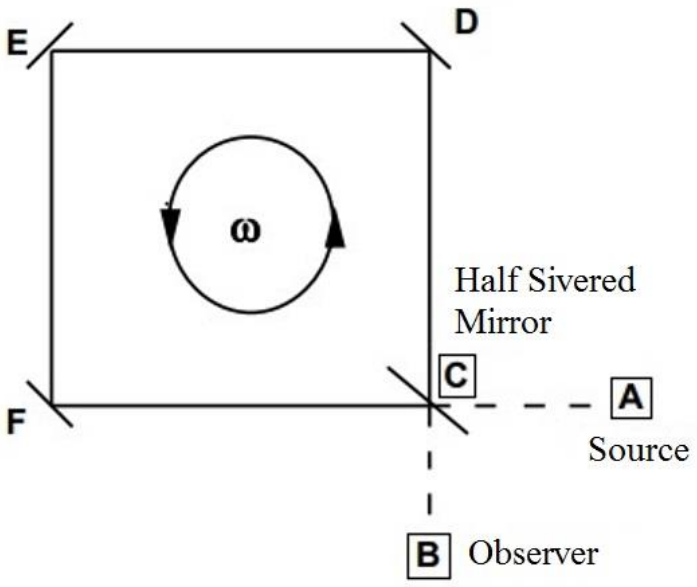


Figure 2.5 Schematic representation of the Sagnac effect [20]

A is the light source which sends the light beam to half-silvered mirror **C**. Since **C** is a half-silvered mirror, some of the light is reflected from it and some of the light passes through it. In other words, some of the light follows the path **C-D-E-F-C-B**, while some of it goes through the path **C-F-E-D-C-B**.

During the experiment the whole system including A and B turns with an angular speed of. The difference in time *dt* for two light beams moving in opposite directions is formulated by Sagnac as follows:

$$dt = 4A\omega/c^2 \qquad \textbf{(2.1)}$$

where ω is the angular velocity in radians per seconds and A is the area enclosed by the light beams.

The fiber optic gyroscope based on the Sagnac effect is shown in Figure 2.6. With the help of the couplers, light coming from the source is split into two equal parts and transmitted to the fiber loop. In the fiber loop, one of the light beams moves clockwise direction while the other moves counterclockwise direction. If the entire system rotates with an angular velocity, then the phase difference between the lights becomes:

$$\Delta\varphi = 8\pi NA\Omega/c\lambda_0 \qquad \textbf{(2.2)}$$

where N is the number of fiber turns in the Sagnac sensing coil loop, A is the enclosed area and λ_0 is the free space wavelength [22].

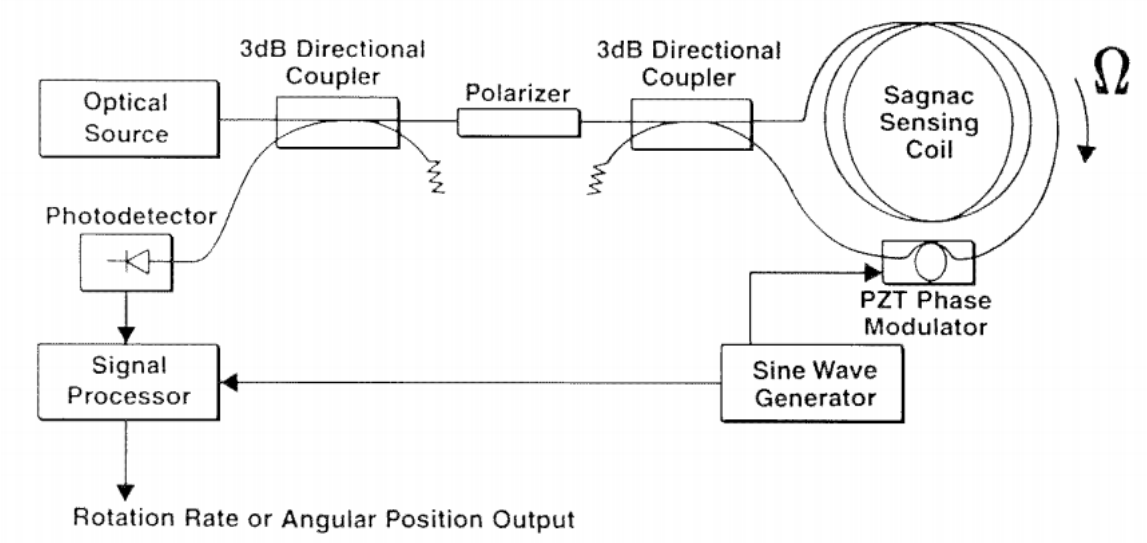


Figure 2.6 The schematic representation of a fiber optic gyroscope based on the Sagnac effect [21]

2.1.2.3 MEMS Gyroscopes

Like the other types of gyroscopes, MEMS gyroscopes are also used to detect and measure the angular motion of an object in three different axes. The advantage of MEMS sensors

is that they are light in weight, small in size and low in cost. However, their performance is much lower than mechanical gyros due to the presence of bias errors.

MEMS gyros integrate the measured angular rate with respect to time in order to detect the attitude of the vehicle on which it is mounted. However, in this integration process the errors are also summed up and at the end the result becomes imprecise. In low cost MEMS gyroscopes, it is possible to see this effect is in a high rate [23].

In most of the MEMS gyroscopes a vibrating mechanical part is employed as a sensing component in order to detect the angular velocity. Unlike the mechanical gyroscopes containing rotating disc as a sensing element, MEMS gyros do not have rotating parts. As a result of this, they can be miniaturized easily.

MEMS gyros with vibrating component detect the angular rotation with the help of the Coriolis effect. This effect is first defined by Gustave-Gaspard Coriolis in 1835 [24]. The Coriolis force can be defined as the force that an object moving on a rotating system experiences perpendicular to its direction of movement. This force is directly proportional to the angular velocity.

For better understanding of the Coriolis effect, it is possible to consider an object with mass m and velocity *v* as represented in Figure 2.7. While the particle moves along the positive y axis, if the system on which it moves starts rotating with the angular velocity of as in the Figure 2.7, the observer fixed on the z axis sees the object moving along the positive z axis. The acceleration of the particle along the z axis which is called Coriolis acceleration is

$$a = 2v\Omega \qquad \textbf{(2.3)}$$

where Ω is the angular velocity of the system and v is the velocity of the object. Although there is no external force applied on the particle, acceleration of the particle along z axis is caused by the Coriolis Force.

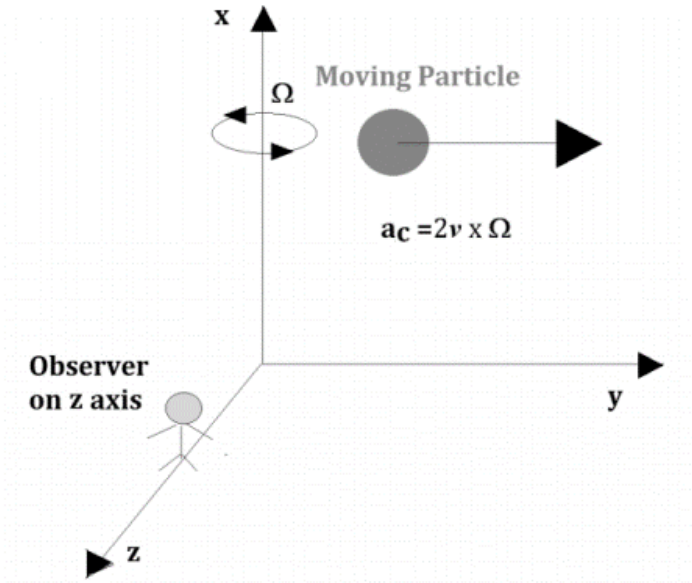


Figure 2.7 Coriolis force on a moving particle [25]

In order to understand the basic mechanism of MEMS gyroscopes it is beneficial to use the following analogy described in Figure 2.8.

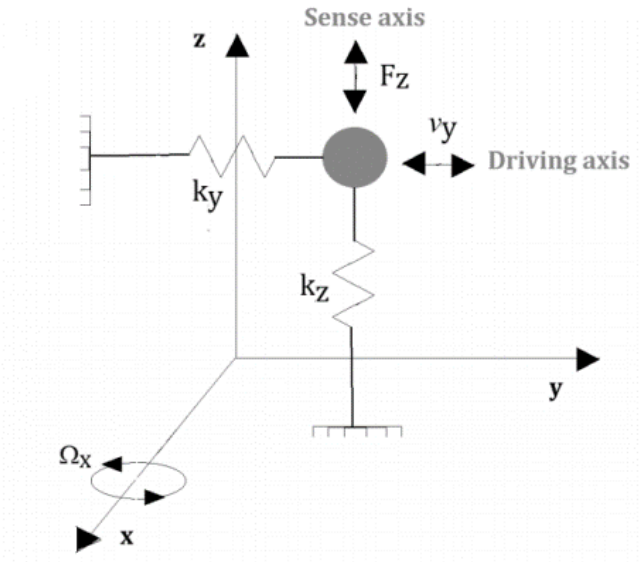


Figure 2.8 Basic MEMS gyroscope principle [25]

MEMS gyroscopes containing vibrating element have two axes along which the vibrating component used for sensing can move. In the analogy of Figure 2.8, k_y and k_z are spring constants. In such a system it is possible to write the following equations [26]:

$$m\ddot{y} = -k_y y - c_y \dot{z} + F_{Drive} \quad \textbf{(2.4)}$$

$$m\ddot{y} = -k_z z - c_z \dot{z} + F_{C_z} \quad \textbf{(2.5)}$$

$$F_z = |2m\Omega| \quad \textbf{(2.6)}$$

where c_y and c_z are the damping coefficients. The motion along y axis which is called drive axis is started with the effect of F_{Drive} as in Eq. 2.4. On the other hand, Eq. 2.5 shows the motion along z axis (sense axis) caused by the Coriolis force F_{C_z}.

Scanning electron micrograph (SEM) of an example MEMS gyroscope designed by Jiang et al. is shown in Figure 2.9 [26], [27].

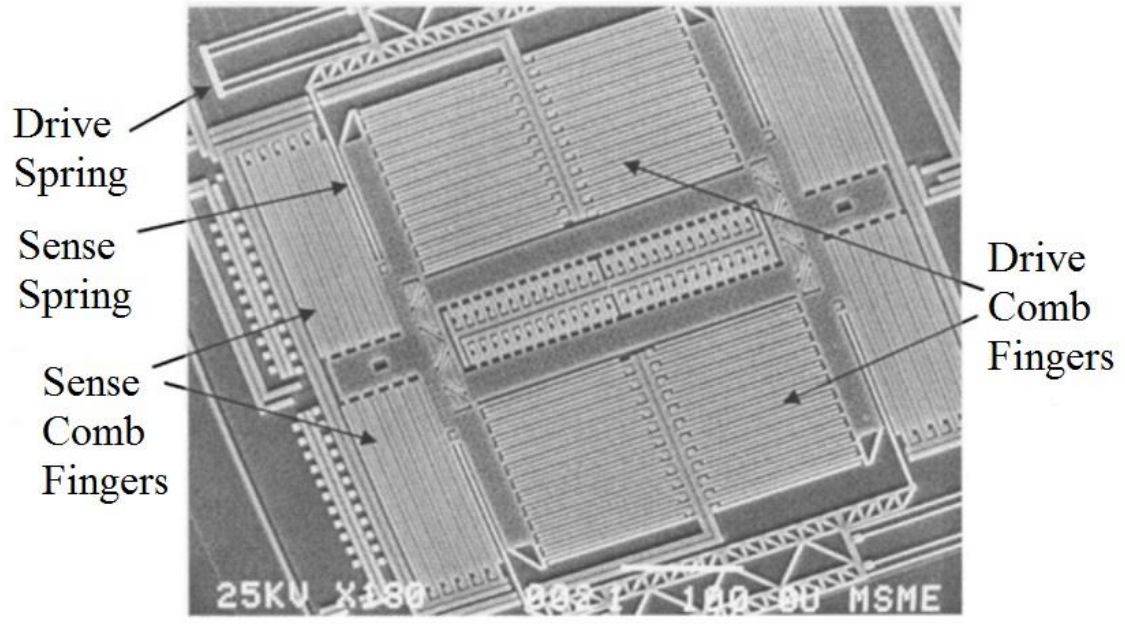


Figure 2.9 SEM of a z-axis vibratory gyroscope with digital output [26]

2.1.3 Accelerometer

Accelerometer can be defined as a device measuring the physical acceleration felt by an object [28], [29]. Although there are a lot of accelerometer types, in general it is possible to divide them into three groups: mechanical, optical fibre and MEMS accelerometers. In this section, first a short discussion of mechanical accelerometers is given to better understand the basic operation principles of the accelerometers. Then the other types of accelerometers are presented briefly.

2.1.3.1 Mechanical Accelerometers

As stated by Newton's second law which is $F = ma$, there is a direct relation between the acceleration of a rigid body, a, and the mass of it, m. By using this relation, it is possible to detect the acceleration of an object if the force, F, acting upon it is known. The most basic principle upon which accelerometers based is this relation between force and acceleration. In the simplest form, an accelerometer contains a mass mounted on the object whose acceleration is to be detected via the springs as represented in Figure 2.10.

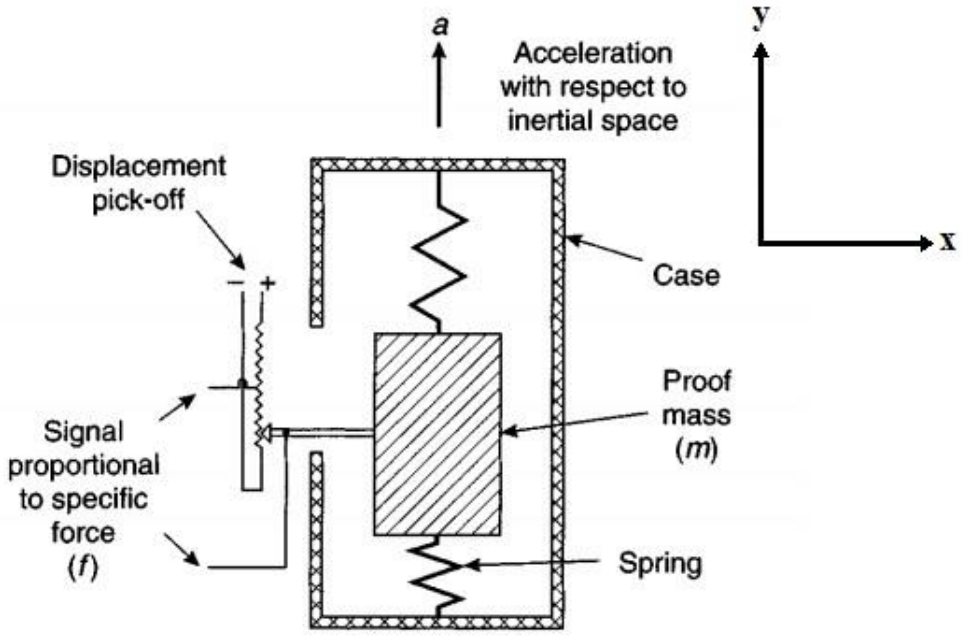


Figure 2.10 Simple mechanical accelerometer [18]

In Figure 2.10, the sensitive axis of the accelerometer is y axis. It means that if the object accelerates along this axis it is possible to measure its acceleration. In this case,

$$F = ma = mf + mg \quad \textbf{(2.7)}$$

where *f* is the acceleration occurred due to the forces other than gravity.

Another type of mechanical accelerometer is *force-feedback pendulous accelerometer* where optical, inductive or capacitive techniques are applied to detect the acceleration. In this type of mechanical accelerometers, a motion along the sensitive axis of a mass mounted on the object whose acceleration is to be measured is detected with the help of the mentioned techniques. In optical technique, acceleration is measured by detecting the amount of light beam changes with the motion of the mass. In inductive technique, by measuring the change in the mutual inductance of the coils caused by the motion of the mass the acceleration is detected as in Figure 2.11. In capacitive case, the motion of the mass causes a change in the capacitance which used to find the acceleration of the object.

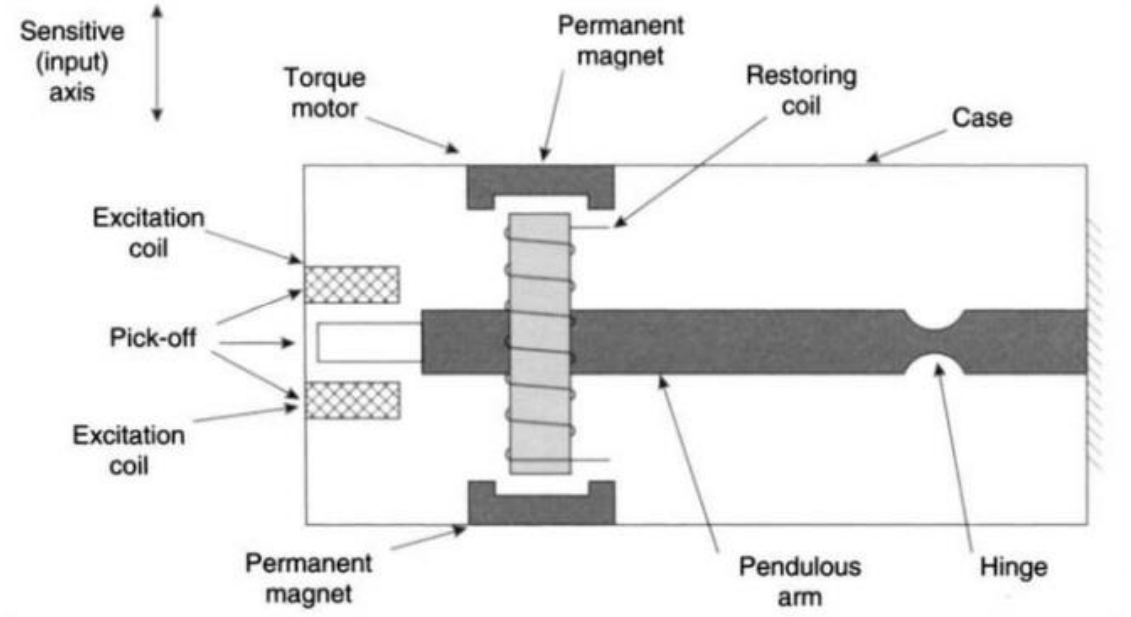


Figure 2.11 Force-feedback pendulous accelerometer [18]

2.1.3.2 Optical Fibre Accelerometers

As its name indicates, fiber optic cables are used to measure the acceleration in this type of accelerometers. The basic principle is similar to the mechanical accelerometers. The pendulum in this case is the fibre optic cable with a mass attached to it itself. When there is motion normal to the fibre optic cable it is deflected. The deflection of the cable is sensed with the help of the laser beam going inside it [18].

Fiber optic accelerometers can provide more accurate measurements than its mechanical counterparts when selected properly. In Figure 2.12 and Figure 2.13, the sensor structure and the functional schematic of a tilting mirror type of fiber-optic accelerometers are illustrated, where two output fibers are used to detect the amount of light changes in case of acceleration.

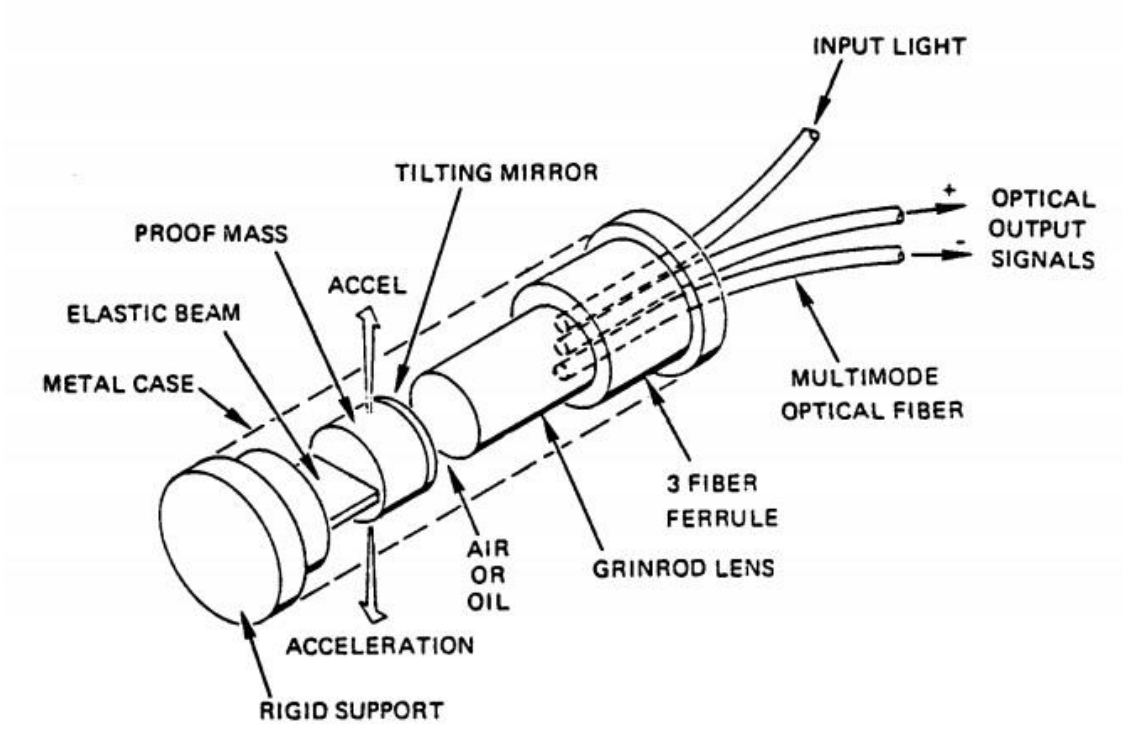


Figure 2.12 The structure of a tilting mirror fiber optic accelerometer [30]

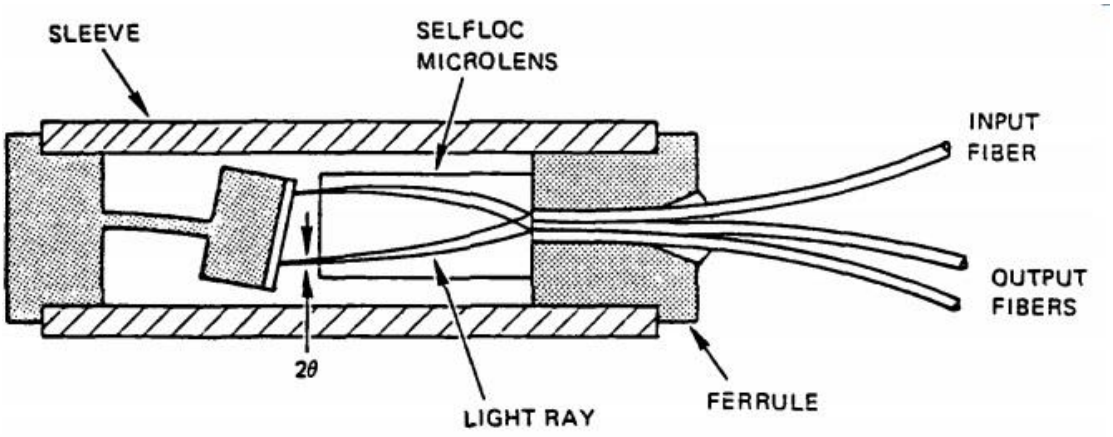


Figure 2.13 The functional schematic of a tilting mirror fiber optic accelerometer [30]

2.1.3.3 MEMS Accelerometers

There are different types of MEMS accelerometers. Some of them are based on piezoelectric effect, where crystal structures are employed to sense the acceleration. When the force caused by the acceleration is applied on the crystal structure, a voltage is generated in proportion to acceleration force. By using the magnitude of generated voltage value, it is possible to measure the acceleration of a moving object.

Another type of accelerometer works on the principle of sensing the change in a capacitance value [31]. This type of MEMS accelerometers includes a proof mass with springs mounted on the substrate which can move on a specific axis [32]. When the object moves along that axis the proof mass moves due to the force of acceleration. This cause a change in the capacitance of the capacitors placed on the structure of the accelerometer. Figure 2.14 shows the structure of this type of MEMS accelerometer [33].

If three MEMS accelerometers are used in three different axes x, y and z, it become possible to sense the acceleration in three axes. Figure 2.15 and Figure 2.16 show the structure and electronic circuitry of a three-dimension (3D) MEMS accelerometer respectively [34].

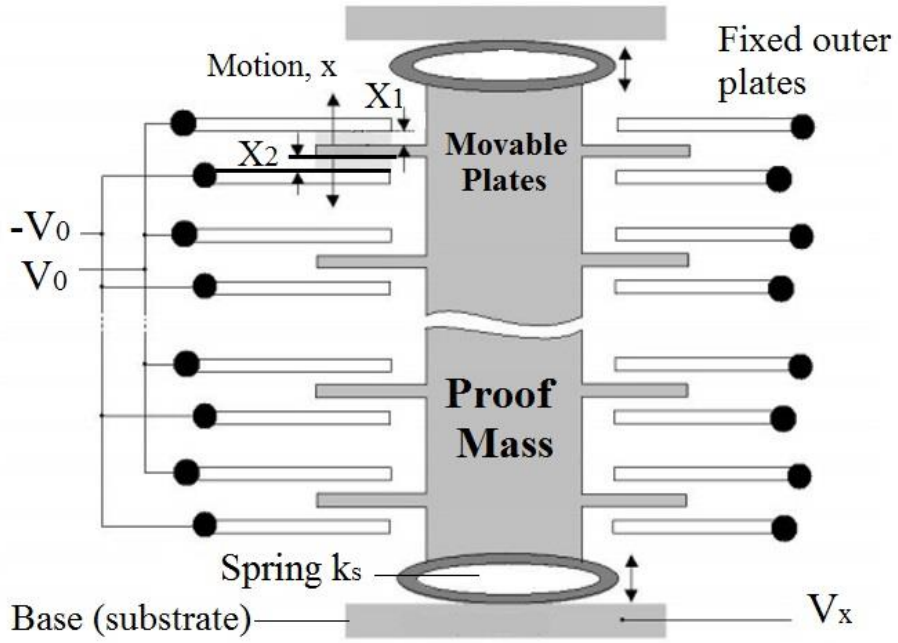


Figure 2.14 MEMS accelerometer structure [33]

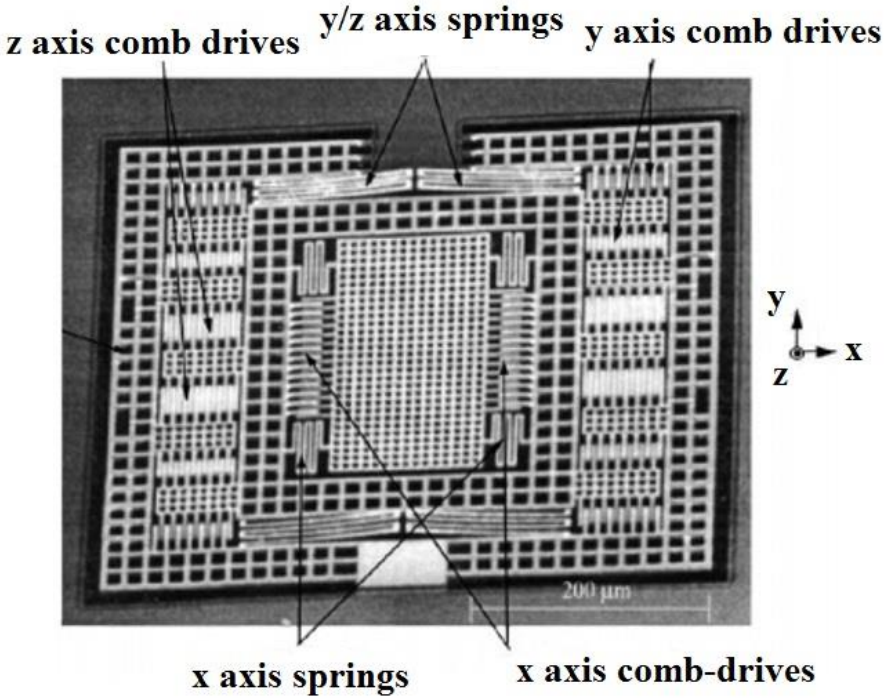


Figure 2.15 Structure of a 3D MEMS accelerometer [34]

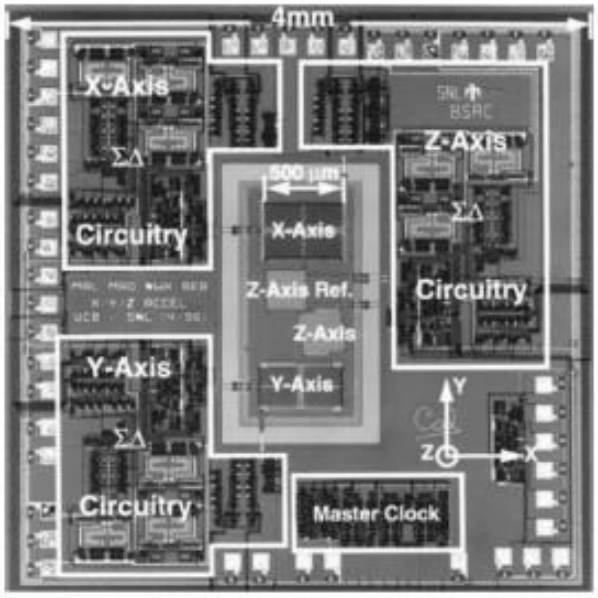


Figure 2.16 Electronic circuitry of a 3D MEMS accelerometer [34]

2.2 Fundamental Principles of INS

In this section basic terminologies and useful concepts that help in understanding the inertial navigation system mechanism are explained briefly. First, basic information regarding reference frames is given in Chapter 2.2.1. Then in Chapter 2.2.2, direction cosine matrix (DCM) is reviewed. Finally, in Chapter 2.2.3, basic operation principles of inertial navigation systems are discussed.

2.2.1 Reference Frames

One of the most critical concepts in inertial navigation is reference frames. In different circumstances different reference frames can be used. Therefore, it is of utmost importance to know the difference between the reference frames. In this chapter, the four most used reference frames in navigation are explained, which are *inertial frame, Earth frame, navigation frame* and *body frame*.

2.2.1.1 The Inertial Frame (i-frame)

The inertial frame, in short i-frame, can be defined as a stationary frame of reference which stands still as the Earth rotates. The origin of the inertial frame is taken as the center of the Earth [35]. Three axes of inertial frame, x_i, y_i and z_i are shown in Figure 2.17.

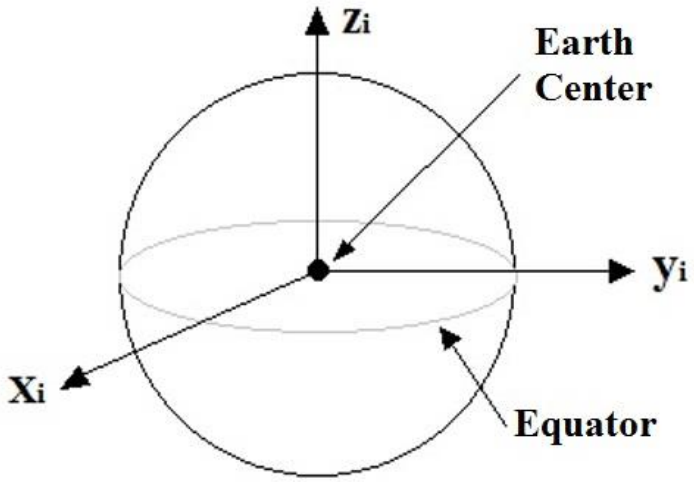


Figure 2.17 The inertial frame (i-frame)

2.2.1.2 The Earth Frame (e-frame)

Like the inertial frame, the origin of the Earth frame is at the center of the Earth as well. Axes of the Earth frame are called x_e, y_e and z_e. The x_e axis passes through the intersection point of the equator and the Greenwich Meridian. Unlike the inertial frame, which is stationary, Earth frame turns around the z_i axis with the rotation of the Earth.

The Earth frame representation is shown in Figure 2.18. Axes pointing towards the north pole are the same for both inertial frame (i-frame) and Earth frame (e-frame) which are z_i and z_e.

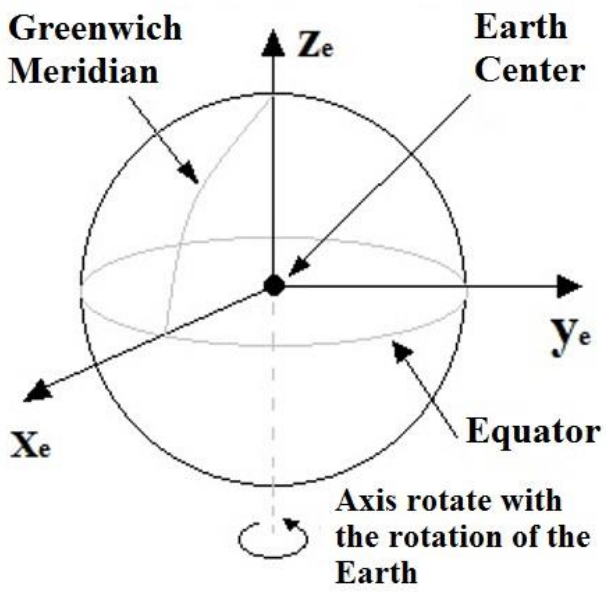


Figure 2.18 The Earth frame (e-frame)

2.2.1.3 The Navigation Frame (n-frame)

Figure 2.19 illustrates the concept of navigation frame and the axes associated with it. The origin of the navigation frame (n-frame) is centered at the location of the navigation system, point **P**. Therefore, this navigation system is used locally. The axes of n-frame are called **N**, **E** and **D** standing for north, east and down respectively.

As stated previously Earth frame rotates at the speed of Earth's spin. On the other hand, n-frame changes its position with the vehicle. Therefore, there is a difference between the n-frame turn rate and e-frame turn rate, which is expressed as ω_{en}.

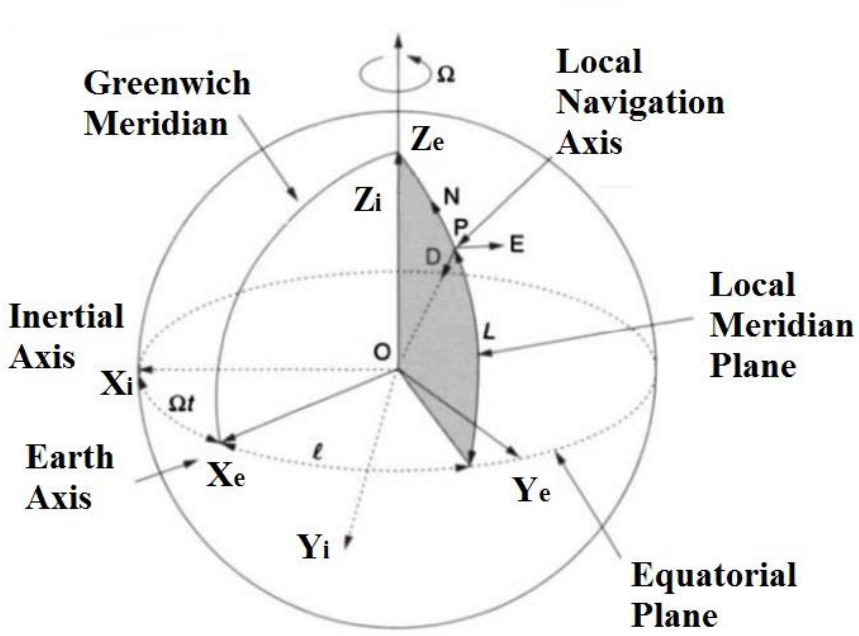


Figure 2.19 The inertial frame, earth frame and navigation frame on the same figure [18]

2.2.1.4 The Body Frame (b-frame)

The body reference frame is centered at the body of a vehicle. Inertial sensors, gyros and accelerometers, on a strapdown inertial navigation system measure the motion of the b-frame with respect to the i-frame. Therefore, body frame is used at the first step of the navigation. Then using direction cosine matrix which is explained in Chapter 2.2.2, transition between the reference frames is executed.

Orthogonal axes of the body frame are shown in Figure 2.20, which are entitled as x_b, y_b, and z_b [18]. This set of axes is aligned with the roll, pitch and yaw axis of the vehicle as represented in Figure 2.21.

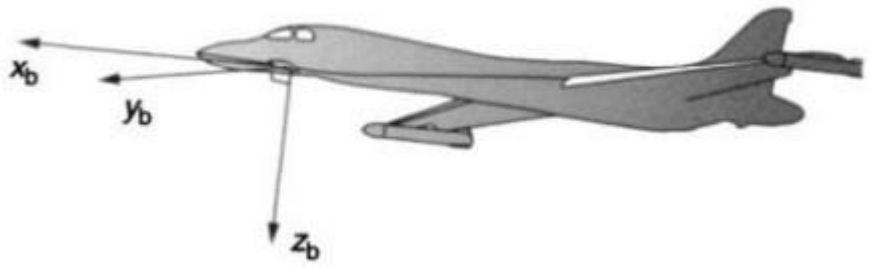


Figure 2.20 Orthogonal axis of the body frame [18]

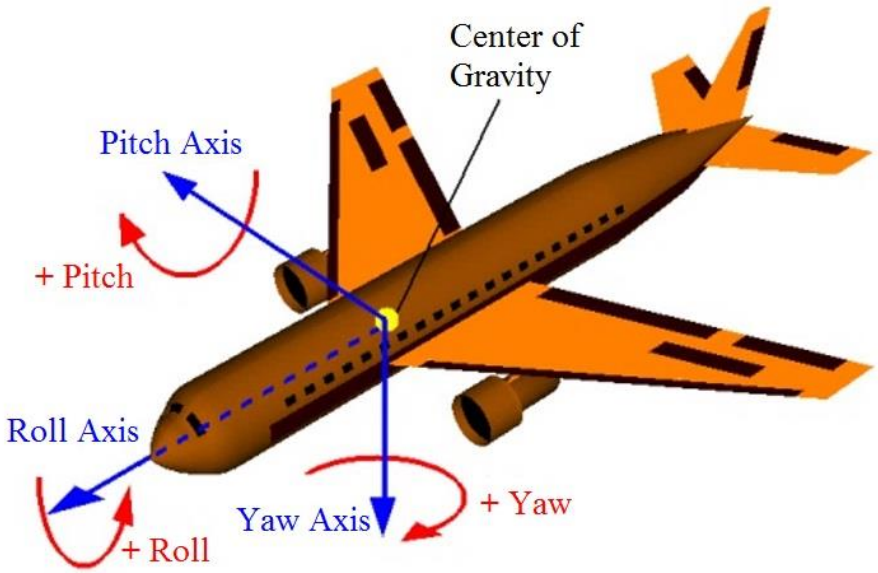


Figure 2.21 Roll, pitch and yaw axis of the vehicle [54]

2.2.2 Direction Cosine Matrix (DCM)

The measured data coming from the inertial sensors expressed in body frame as roll, pitch and yaw angles. This measured body frame data only provides information about the instant movements of the object, and no information is given regarding the position of the object. In order to detect the vehicle position and attitude correctly, it is necessary to convert the body frame data provided by accelerometers and gyroscopes into other reference frames. When body frame is transformed to other reference frames such as navigation frame or Earth frame, it becomes possible to locate the position of the vehicle.

The reference frame conversion is performed using a transform matrix, called direction cosine matrix or in short DCM. The formation of direction cosine matrix changes for different circumstances. In the following, a simple example is given to clarify reference frame conversion process.

Let the data set coming from an accelerometer be f_b. As explained in Chapter 2.1.3, inertial accelerometers first measure the force with the help of the proof mass mounted on it. Then this force value is used to calculate acceleration. Since the first step begin with the force measurement, data coming from the accelerometer is stated as *f*. Superscript *b* tells that the data is expressed in *body frame.* In order to convert the data in body frame to inertial frame f^b is to be multiplied by direction cosine matrix as follows [18]:

$$f^i = C_b^i * f^b \tag{2.8}$$

where f^i is the converted version of the data coming from the accelerometer. Superscript *i* means that the data is expressed in inertial frame of reference. C_b^i is the direction cosine matrix used to convert the accelerometer data from body frame to inertial frame. DCM used here is a 3x3 matrix consisting of the attitude values of the vehicle; in other words, the attitude of the body frame with respect to the chosen reference frame, which in this case is inertial frame.

C_b^i matrix is calculated from the attitude vector, $\omega_{ib}^b = [\text{p q r}]^T$, coming from the gyroscopes. In the vector ω_{ib}^b, superscript *b* tells that the data is expressed in *body frame* and subscript *ib* means that the attitude of the vehicle body frame with respect to the inertial reference frame. With the help of the ω_{ib}^b, the skew symmetric matrix Ω_{ib}^b is defined as follows [18]:

$$\Omega_{ib}^b = \begin{bmatrix} 0 & -r & q \\ r & 0 & -p \\ -q & p & 0 \end{bmatrix} \tag{2.9}$$

Finally, direction cosine matrix, C_b^i, which is used to convert data from the body frame expression to the inertial frame expression is obtained as in Eq. 2.10.

$$\dot{C}_b^i = C_b^i * \Omega_{ib}^b \quad \textbf{(2.10)}$$

where $\dot{C}_b^i$ is the time derivative of the matrix C_b^i. Transition between reference frames may be conducted by using different methods. Further information regarding the other methods is available for enthusiastic readers in [18].

2.2.3 Inertial Navigation System Mechanism

Navigation, in general, is an operation of detecting the position, attitude and velocity of a vehicle according to pre-determined frame of reference. Inertial navigation does the same task by using the data coming from the inertial sensors mounted on a vehicle without relying on any external references. For this purpose, most of the navigation systems must perform the following tasks [36]:

- Have inertial sensors used to obtain attitude data
- Have inertial sensors used to obtain velocity data
- Know the gravitational field
- Time integrate the obtained data from the inertial sensors

The task of finding attitude is performed by the gyroscopes mounted on the vehicle. As mentioned in Chapter 2.1.2, gyroscopes are devices used to measure the angular velocity. Gyroscopes, in short gyros, have one sensitivity axis in general. Therefore, in an inertial navigation system it is recommended to have at least three gyros to obtain the attitude data from **x**, **y** and **z** axes.

The next task of determining the velocity is accomplished by the accelerometers, which are the inertial sensors used to measure the proper acceleration of a vehicle. Proper acceleration is defined as the physical acceleration felt by an object. Like the gyroscopes,

accelerometers have a sensitivity axis in general. Therefore, in an INS at least three accelerometers are used to get data from three axes.

In order to understand the operation of gyroscopes and accelerometers in an inertial navigation system it is beneficial to examine the following example representing the two-dimensional inertial navigation system in Figure 2.22.

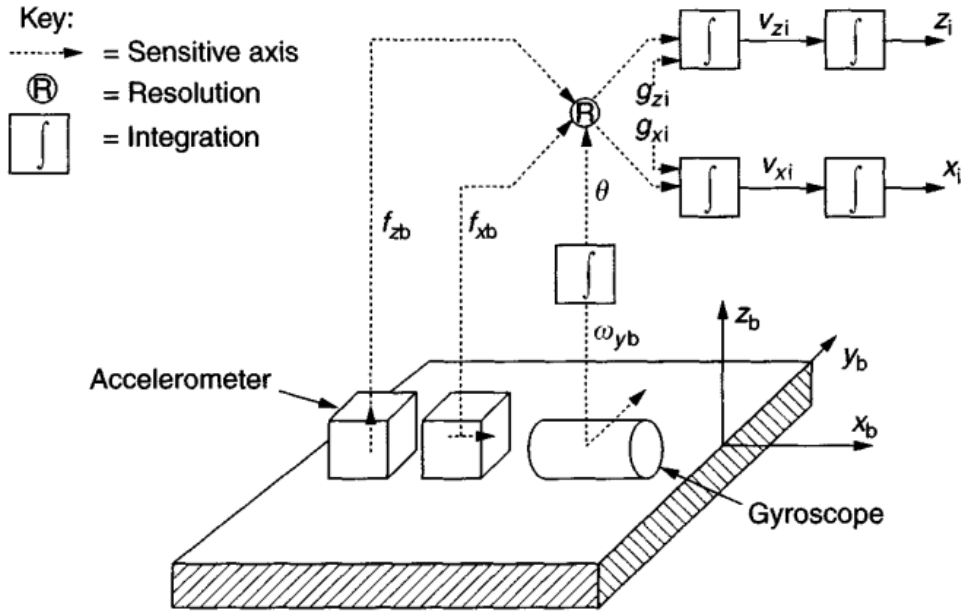


Figure 2.22 Two-dimensional SINS [18]

The SINS in Figure 2.22 has two accelerometers one of which has its sensitivity axis along the **z** axis and the other one along the **x** axis. Therefore, it is assumed that the vehicle is only moving on **xz** plane. It has also one gyroscope whose sensitivity axis is along the **y** axis, meaning that that the turn rate of the vehicle along the y axis is detected by the gyroscope.

A simple motion scenario of the vehicle is decided as in Figure 2.23. Subscript *b* stands for body reference frame while subscript *i* denotes inertial reference frame. Assuming that both reference frames are coincident it can be inferred from Figure 2.23 that the vehicle

turns θ degree from the inertial frame. Relationship between the vehicle position and the b-frame axis is depicted in Figure 2.22

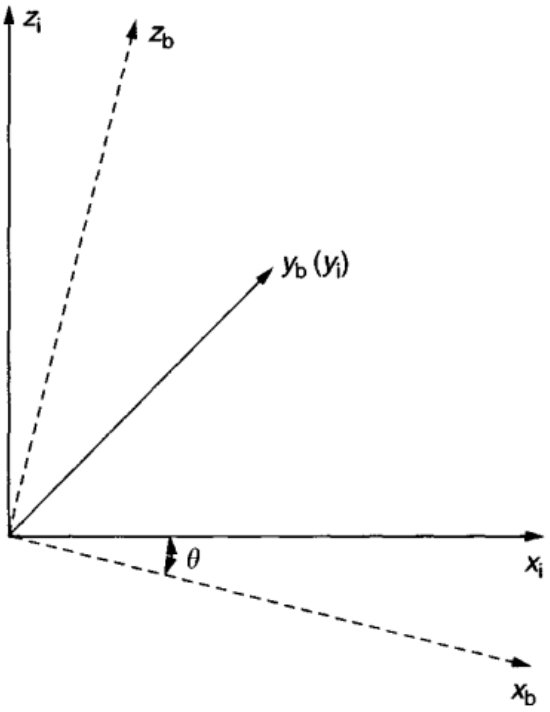


Figure 2.23 Two-dimensional navigation motion scenario [18]

Data coming from the gyroscope mounted on the vehicle is expressed as ω_{yb} which is the angular rate. As can be seen in Figure 2.22, ω_{yb} is integrated to find the overall attitude of the body which is θ.

First data obtained from the accelerometers are in terms of force in Figure 2.22. As explained in Chapter 2.1.3, this force is derived from the acceleration of the body. In order to resolve the forces, attitude data obtained from the gyroscope is used. Inertial navigation operations up to this point can be described by the following equations.

$$\dot{\theta} = \omega_{yb} \tag{2.11}$$

$$f_{xi} = f_{xb}cos\theta + f_{zb}sin\theta \tag{2.12}$$

$$f_{zi} = -f_{xb}sin\theta + f_{zb}cos\theta \quad \textbf{(2.13)}$$

Eq. 2.11 is the integration of the instant angular turn rate data coming from the gyro. Eq. 2.12 and Eq. 2.13 are the resolution of the force data obtained from the accelerometers.

The third task of inertial navigation involves gravitational field. Gravity forces is to be taken into consideration by combining the resolved forces with the gravity component. At this point, the acceleration data is obtained. By integrating this data as in Figure 2.22, velocity data is obtained. Integrating the velocity data, position data is measured as expressed by the following equations.

$$\dot{v}_{xi} = f_{xi} + g_{xi} \quad \textbf{(2.14)}$$

$$\dot{v}_{zi} = f_{zi} + g_{zi} \quad \textbf{(2.15)}$$

$$\dot{x}_i = v_{xi} \quad \textbf{(2.16)}$$

$$\dot{z}_i = v_{zi} \quad \textbf{(2.17)}$$

Although there are many studies involving other factors leading to the modification of the INS equations, the review provided in Chapter 2 is sufficient to understand the fundamentals of an INS system. For further information regarding the extensive studies on various forms of INS equations reader is referred to [18], [37] and the references therein. General block diagram of a strapdown inertial navigation system according to the equations mentioned above can be expressed as in Figure 2.24.

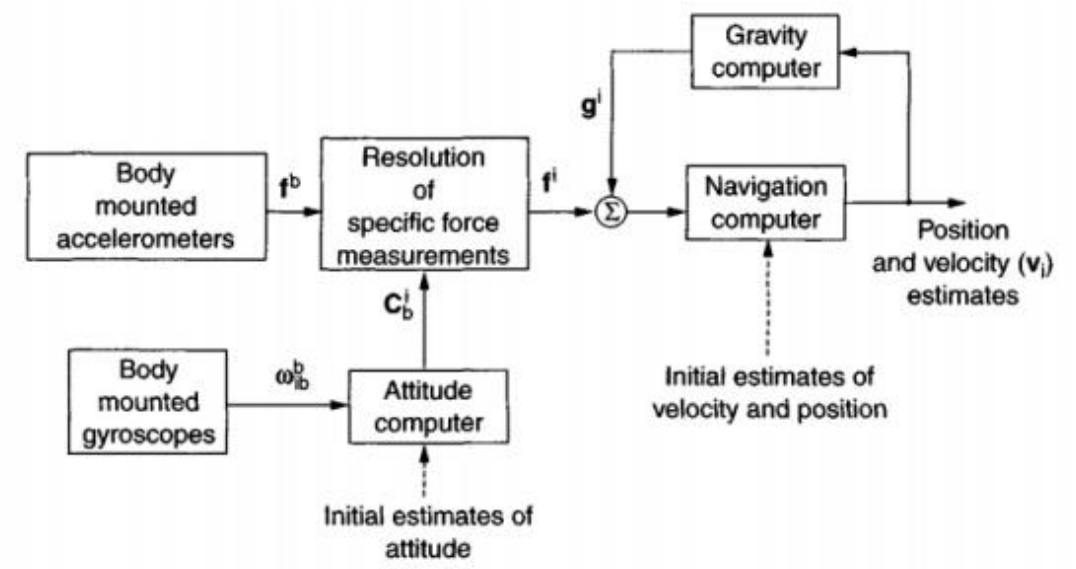


Figure 2.24 SINS block diagram [18]

CHAPTER 3

METHODS USED FOR THE NAVIGATION IN GPS-DENIED ENVIRONMENTS

In this chapter brief information regarding the navigation methods commonly used in GPS-denied environments is given. In Chapter 3.1 Simultaneous Localization and Mapping (SLAM) and in Chapter 3.2 Visual Odometry (VO) is discussed. Lastly, utilizing multiple inertial sensors and inertial measurement units in an inertial navigation system are examined in Chapter 3.3.

3.1 Simultaneous Localization and Mapping (SLAM)

SLAM can be defined as a method or a process where moving objects create the map of the environment in a gradual way and at the same time determine its own position within this environment. In this method there is no need to know the prior location of the object or the map of the environment. SLAM is first presented by H. Durrant-Whyte at the ISSR (International Symposium on Robotics Research) in 1995 and has become an important issue studied over the last years since it facilitates the navigation of mobile robots [38]. Simultaneous Localization and Mapping has also become a useful method for the navigation of the UAVs (Unmanned Aerial Vehicles) in GPS denied environment [39].

One of the most important parts of the simultaneous localization and mapping process is called *landmark selection*. Landmarks are generally objects having characteristic features in the environment so that they can be detected easily by the sensors mounted on the moving object during its travel. These landmarks are used as a reference point during the navigation process. There are two types of landmarks: landmarks defined before the navigation and landmarks defined during the navigation. Before moving to the SLAM process, these two types of landmarks are examined briefly.

As its name implies, pre-defined landmarks are defined before the navigation process starts. This type of landmarks are used in areas where the environment is known, such as buildings. For example, in [40], a mobile tour-guide robot, Minerva, is navigated with this method by using the ceiling lights of the Smithsonian's National Museum of American History as a landmark. The mobile tour-guide robot, Minerva, is shown in Figure 3.1 [40].



Figure 3.1 Mobile tour guide robot, Minerva [40]

Predefined landmarks are useful and highly applicable in environments such as buildings, hospitals, museums etc. However, it is not possible to find this kind of salient and regular landmarks in a lot of environments. Therefore, researchers have developed different algorithms in order to provide that the mobile robot autonomously decide different landmarks in accordance with the environmental situations during its travel. For example, in [41] an algorithm called *BaLL* which is based on *Markov Localization* is developed for this purpose. With the help of *BaLL*, a mobile robot which uses sonar sensors and a camera decides highly useful landmarks during its trip. Another example for autonomous landmark decision is to use computational visual attention system [43]-[45]. In this method Regions of Interests (ROIs), areas that are significant in the environment due to their strong contrast and uniqueness, are used to detect the landmarks. While the camera mounted on a robot capturing, ROI is detected and used for the decision of the landmark by using the process shown in Figure 3.2 [42].

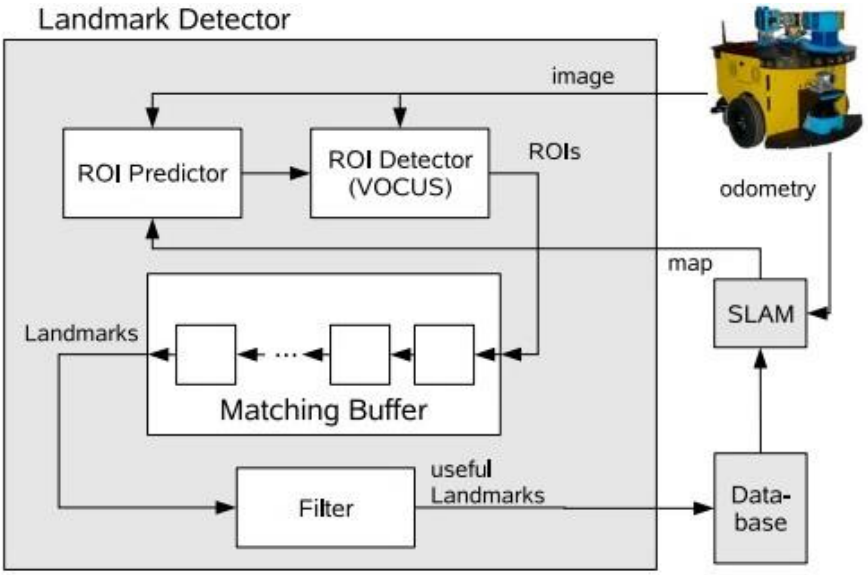


Figure 3.2 Landmark selection for SLAM [42]

Landmarks that are specified before or during the navigation process as mentioned above are used by the robot for relative measurement. At the same time, it creates a map of the environment where it is located while it starts to identify his position in this map. Figure 3.3 sheds light on this concept [38]. At any time, instant *k*, the following vectors are defined for the navigation:

- x_k: state vector expressing the location and attitude of the mobile robot
- u_k: control vector used to direct the robot to state
- m_i: true landmark location
- z_{ik}: estimated landmark location

In addition to the above vectors, history of the above vectors are also collected and saved in order to form the database which are namely as follows:

- $X_{0:k}$: state vector expressing the location and attitude of the mobile robot
- $U_{0:k}$: control vector used to direct the robot to state
- m : true landmark location

- $Z_{0:k}$: estimated landmark location

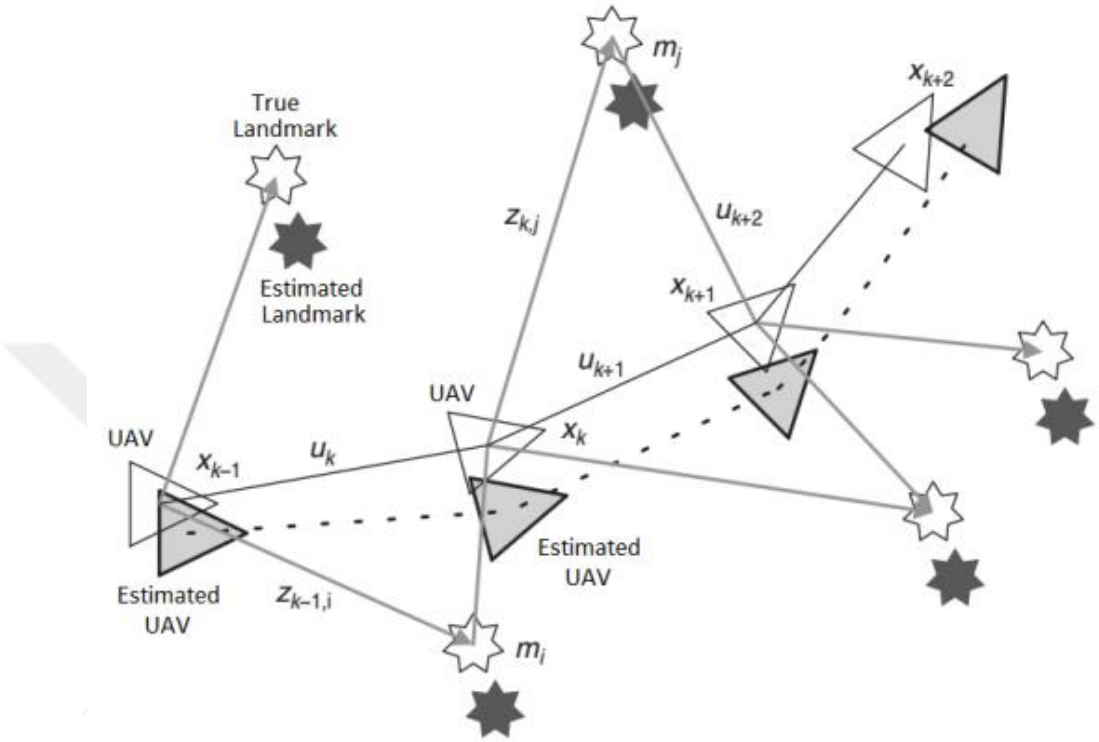


Figure 3.3 SLAM process schematic for a UAV [38]

3.2 Visual Odometry (VO)

VO is a navigation method in which the position of the vehicle is determined by examining the amount of deviation on the images taken by one or more cameras placed on the moving vehicle. The term Visual Odometry was first used in 2004 by David Nister due to the similarity to the wheel odometry, which gradually measures the position of a moving vehicle by summing up the number of turns of its wheels over a specific time [46], [47]. Block diagram of VO is shown in Figure 3.4 [39].

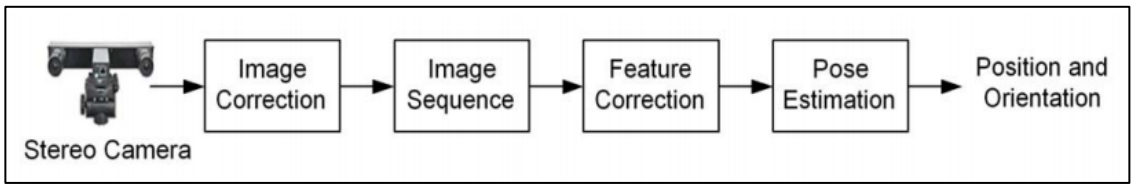


Figure 3.4 Block diagram of visual odometry (VO) [39]

The cameras mounted on a UAV takes pictures sequentially with a period of *k* during its travel as shown in Figure 3.5 [46]. Since a UAV is moving there is a displacement between the images. This displacement is detected incrementally from the image frames taken with the help of the cameras.

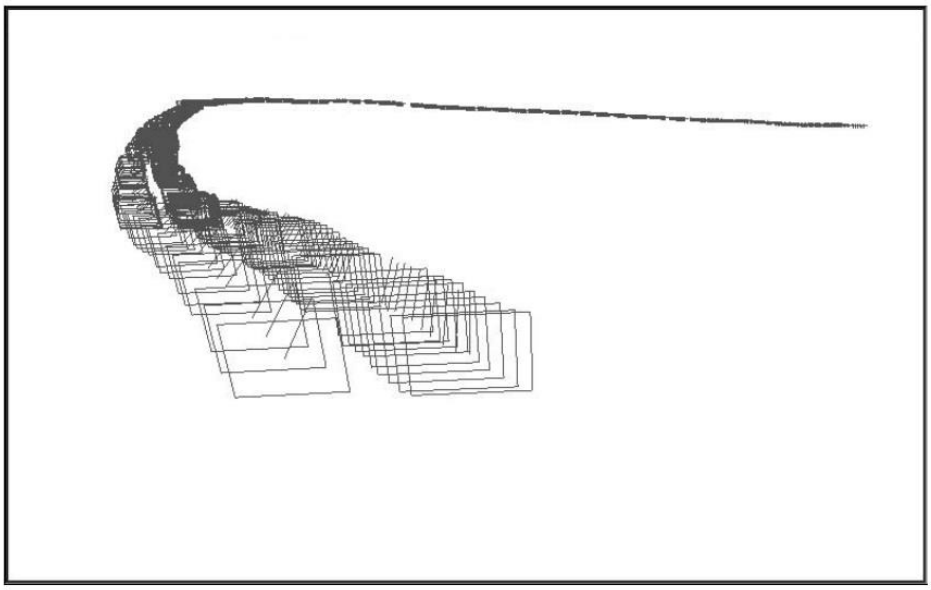


Figure 3.5 Representation of the visual odometry method [46]

If there is only one camera then the set of images taken at times k is represented by $I_{0:n} = \{I_0, \dots, I_n\}$. On the other hand, if the system is a stereo system, meaning that there are two cameras, there should be a left and a right image at each k second, denoted by $I_{l,0:n} = \{I_{l,0}, \dots, I_{l,n}\}$ and $I_{r,0:n} = \{I_{r,0}, \dots, I_{r,n}\}$ as illustrated in Figure 3.6 [47].

Although the reference frame of the vehicle and the reference frame of the cameras are different, for simplicity they are assumed to be the same. All subsequent motions of the UAV is expressed as $T_{1:n} = \{T_{1,0}, \dots, T_{n,n-1}\}$. and the transformation of it is conducted as follows:

$$T_{k,k-1} = \begin{bmatrix} R_{k,k-1} & t_{k,k-1} \\ 0 & 1 \end{bmatrix} \quad \textbf{(3.1)}$$

where $R_{k,k-1}$ is the rotation matrix and $t_{k,k-1}$ is the translation matrix.

Camera pose set is expressed as $C_{0:n} = \{C_0, \dots, C_n\}$, including the transformations of the camera with respect to the initial coordinate frame at k=0. *Cn*, representing the current pose, is computed by combining all the transformations as $T_{1:n} = \{T_{1,0}, \dots, T_{n,n-1}\}$.

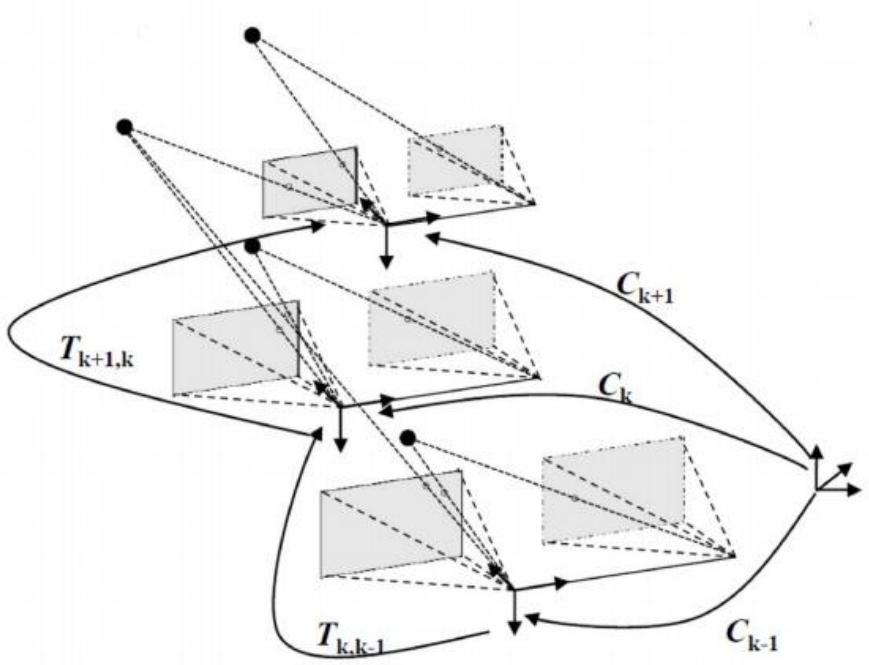


Figure 3.6 An illustration of the VO method [47]

Another method used for the navigation in GPS-denied environment is Laser Odometry (LO). It is similar to Visual Odometry. However, in this case sequences of laser scans are

used for the navigation instead of images sequence. Since the overall principle of LO is similar to VO, it is not explained here. For further detail regarding Laser Odometry reader is referred to [48], [49].

In addition to the above-mentioned methods, a new navigation method in GPS-denied or GPS-degraded regions is proposed in [39], by combining Visual Odometry navigation data with the IMU data as shown in Figure 3.7. It is represented according to the GPS-degraded environment. If the region is GPS-denied, there would not be any GPS data.

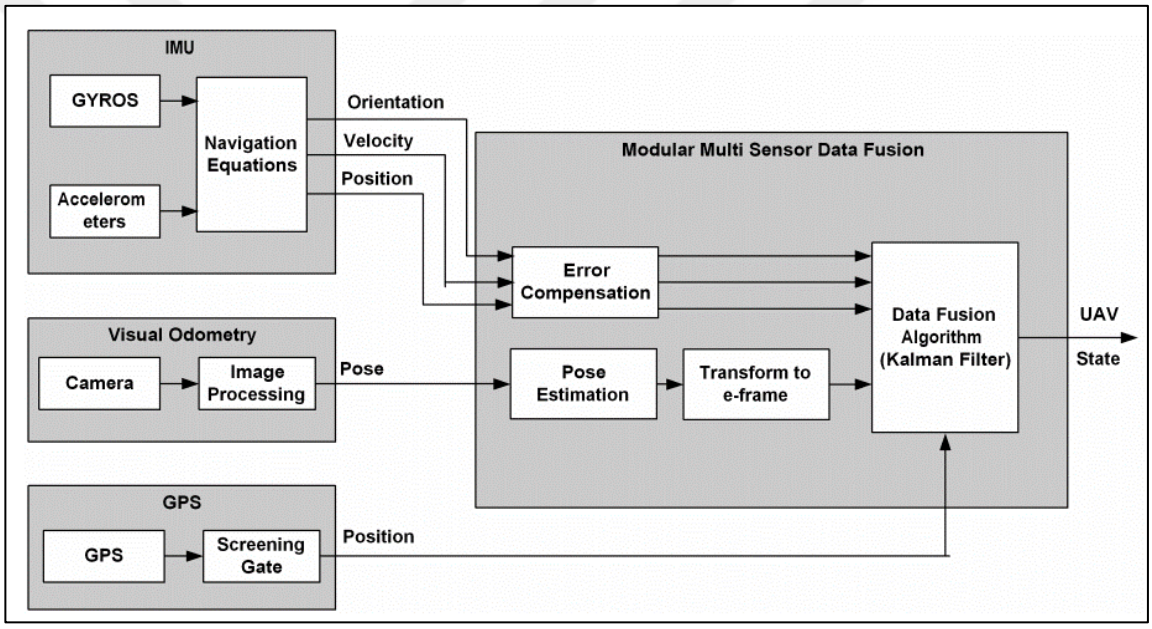


Figure 3.7 Block diagram of the combination of IMU and VO data [39].

3.3 Utilizing Multiple Inertial Sensors and Multiple IMUs

As mentioned in Chapter 1.1, although there are different types of inertial sensors such as mechanical and fiber optic sensors, due to their small sizes and lightweights MEMS sensors have found a great place in inertial navigation systems for UAVs. MEMS inertial measurement units consisting of MEMS inertial sensors are one of the most important parts in a strapdown inertial navigation system for unmanned aerial vehicles [1]. However, the error profiles of MEMS sensors are worse than their mechanical or optical counterparts

and when GPS is unavailable, INS systems become highly unreliable. In Chapter 3.1 and Chapter 3.2, two methods, SLAM and VO, for helping navigation in GPS denied regions have been reviewed. However, these methods rely on image processing and thus require extensive signal processing. In this section, a simpler and computationally efficient method, which utilize multiple IMUs to minimize error profiles of MEMS sensors is examined for navigation in GPS denied environments.

When using multiple IMUs, data coming from multiple inertial sensors is combined in order to obtain better result in comparison with a single sensor. For example, in [8], the output data of four gyroscopes are combined using a suitable Kalman Filter (KF) virtually. It is showed that the accuracy of the virtual gyroscope which uses the multiple data is about 170 times better than an individual gyroscope. In order to visualize the positive effect of using multiple gyros, one of the graphical results in [8] showing the change of the gyroscope drift is illustrated in Figure 3.8.

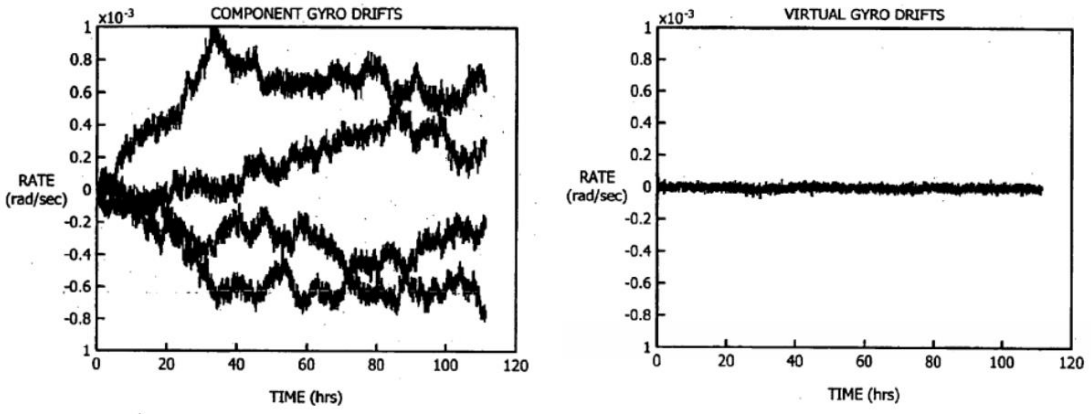


Figure 3.8 Individual gyroscope drifts (left), drift of the virtual gyroscope (right) [8]

In [9], multiple gyroscopes are combined by using the optimal KF proposed in [8] as shown in Figure 3.9. As a result, it is reported that three gyroscopes with a bias drift of 35 degree per hour can be reduced to 0.53 degree per hour by optimally combining them.

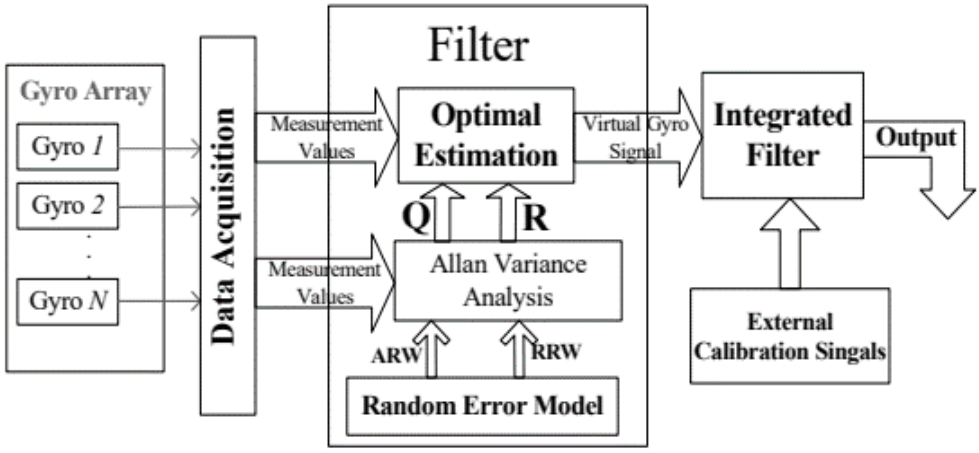


Figure 3.9 Block diagram of the proposed multiple gyroscope method in [9]

In [10], 100 MEMS inertial sensors are combined for the navigation of an unmanned aerial vehicle in a GPS-denied environment. The system also includes two digital signal processors. The type of a filter that is employed in this navigation system is Sigma-point Kalman filter. Overall system is shown in Figure 3.10 [10]. It is stated that the performance of the hardware, if it is properly combined, is close to or even better than a fiber optic inertial sensor.

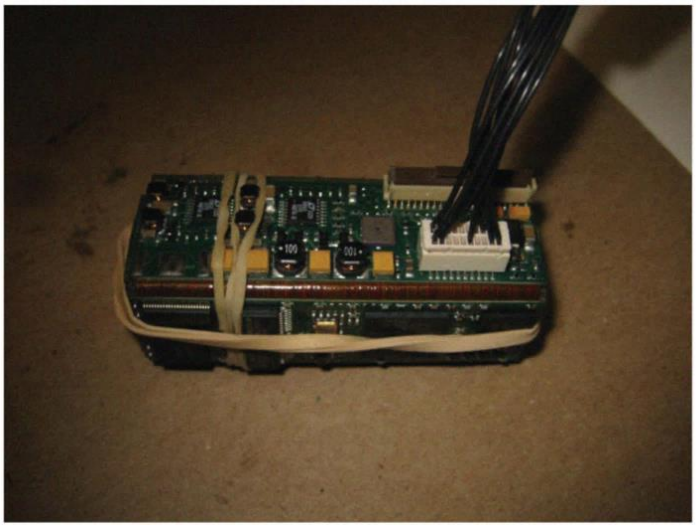


Figure 3.10. Navigation system containing 100 inertial sensors with two digital signal processors [10]

In addition to the above-mentioned methods where multiple inertial sensors are used together, the method of using multiple IMUs to reduce the effect of the error profile of the MEMS sensors is also studied in literature. For example, in [4], it is reported that by employing orthogonal orientation and skew-redundant configuration of MEMS-IMUs as shown in Figure 3.11 the maximum errors are reduced up to a factor of 2.

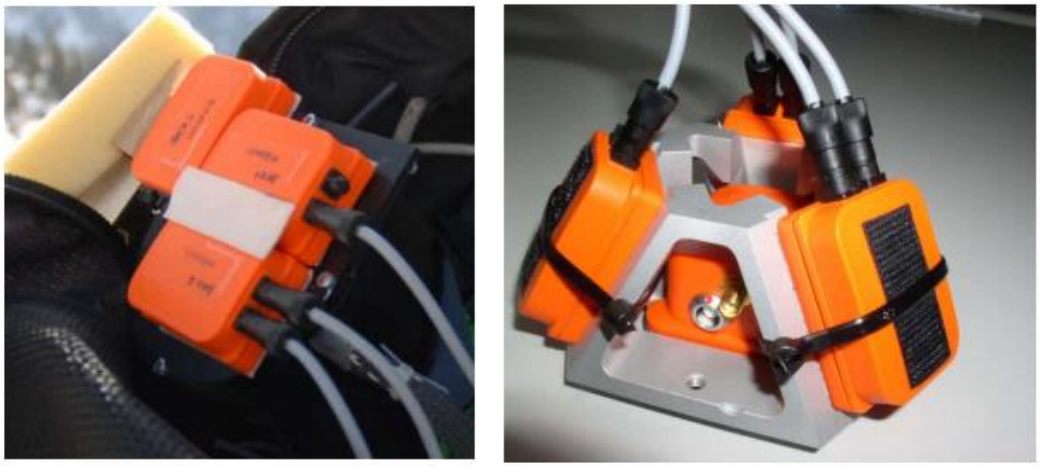


Figure 3.11 Orthogonal configuration (left), skew-redundant configuration (right) for redundant-IMU applications [4]

In [3], a study about improving accuracy with multiple sensors is conducted and the effect of different configurations of MEMS-IMUs on the error profile is examined for various number of IMUs. It is stated that for systems with large redundancy (i.e. 4 or more IMU triads), the most suitable configuration is the orthogonally-redundant IMU configuration. The important point is the fact that this kind of multiple IMU applications are generally used with a GPS aid.

For GPS-denied or GPS-degraded region applications, an embedded IMU platform is designed by using 18 *MPU9150 IMUs*. *MPU9150 IMU* is a 9-axis IMUs and it is depicted in Figure 3.12 [11]. It is shown that the Allan standard deviation, which is used for the analysis and modeling of inertial sensors [55], is reduced by roughly a factor of 3.7 when 14 IMUs are working actively in the system.

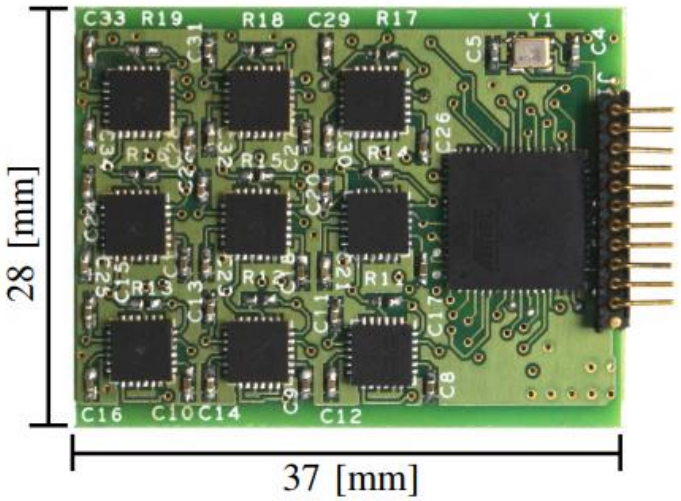


Figure 3.12 The embedded MIMU platform consisting of 18 IMUs [11]

In [12], a new method for combining outputs of multiple IMUs is suggested by implementing four *MPU9150 IMUs* as shown in Figure 3.13. It is presented that ARW coefficient decreases to $0.0022^o/\sqrt{s}$ and VRW error is reduced by %50. In addition, it is stated that standard deviation of the combined system is reduced six times in comparison with a single sensor in dynamic tests. It is further asserted that Steady State Kalman filter is suitable for this kind of multiple IMU applications.

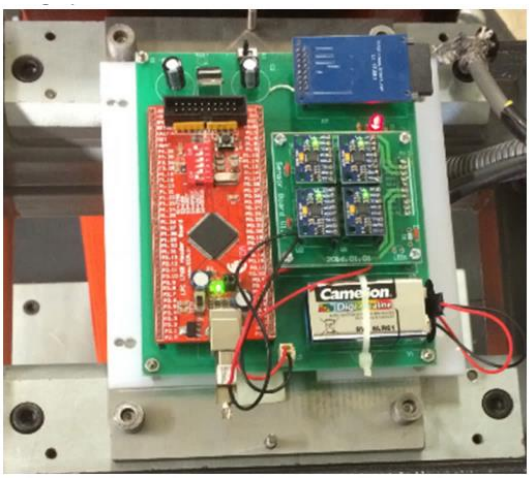


Figure 3.13 Multiple IMU system consisting of four MEMS IMUs [12]

All of the works mentioned in this chapter shows that utilizing multiple inertial sensors in an inertial measurement unit or employing multiple inertial measurement units in an inertial navigation system is an attractive method to reduce the error profile of the inertial navigation. However, in [8], [9] and [10] emphasis is put on the combination of inertial sensors rather utilization of multiple IMUs. In [3] and [4] multiple IMU systems are employed with a GPS aid rather than testing them in a GPS-denied region. In [11] and [12] same type of IMUs, *MPU9150,* are used to design a multiple IMU navigation system. In this thesis, the positive effect of using three different types of IMUs as a multiple IMU INS on the error profile of the navigation system in a GPS-denied environment is examined by using NaveGo, a simulation framework for low-cost integrated navigation system [2].

CHAPTER 4

COMPARATIVE STUDY OF SINGLE AND MULTIPLE IMU SINS IN A SIMULATION ENVIRONMENT

In this chapter comparison between the performances of single and multiple IMU inertial navigation systems are examined. In Chapter 4.1 methodology of the simulation is explained and brief information regarding the simulation environment are given while in Chapter 4.2 simulation process and results are discussed.

4.1 Methodology

In order to conduct a comparative study in a simulation environment between the error profiles of a single and multiple IMU strapdown inertial navigation systems (SINSs), one of the most important needs is to use a suitable simulation framework. In this study, NaveGo, an open source simulation framework for low-cost integrated navigation systems developed in MATLAB, is used as a simulation environment [2]. Before moving on to the comparative simulation results, brief information regarding the NaveGo simulation framework is given in Chapter 4.1.1.

General simulation methodology of this study can be explained as follows. First, true input data expressing the trajectory of the vehicle is defined in the simulation environment. True input data can be obtained either as a real data coming from a real vehicle in motion or as a synthetic data which is entered by the user into simulation framework. In this thesis synthetic data is used as a true input data as explained in Chapter 4.2.1. Then this trajectory data is used as an input of the different inertial navigation systems formed by changing the different features of the NaveGo navigation systems such as filter type, IMU type, GPS error rates etc. Finally, position estimation performances of the inertial navigation systems are plotted on the same graph as an output of the simulation.

Block diagram of the simulation strategy is depicted in Figure 4.1. In this study since the differences between the different navigation systems are caused only by the different IMU configurations, different inertial navigation systems are represented as *IMU1-ErrorProfile, IMU2-ErrorProfile* etc. in Figure 4.1.

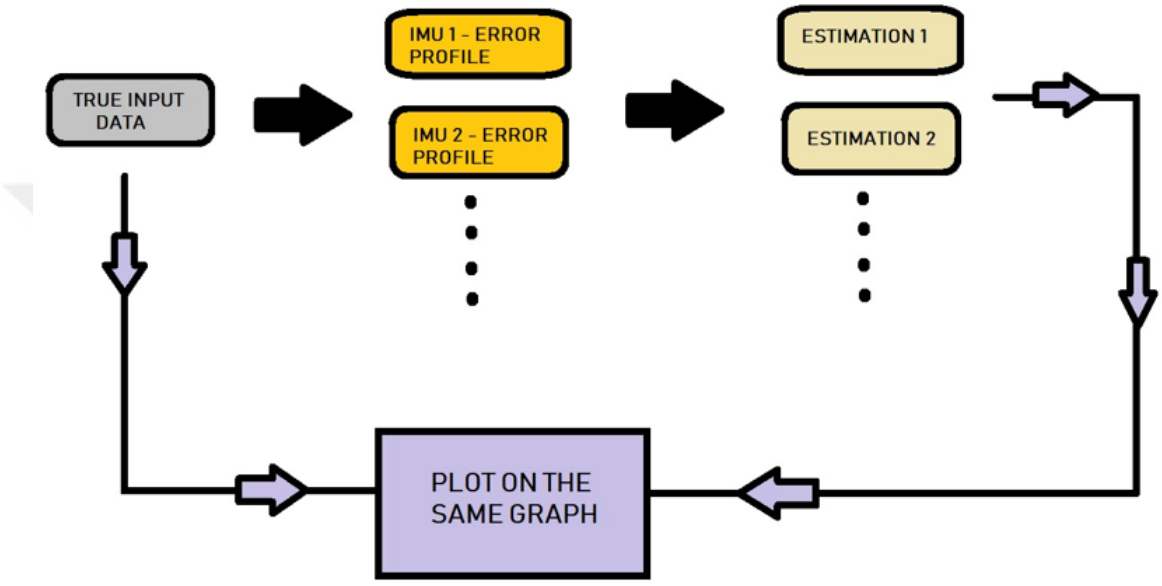


Figure 4.1 General simulation strategy

4.1.1 Simulation Framework

The real trajectory of the vehicle is produced under the name of *true input data* in NaveGo as follows:

$$T = [\, e, p, v^n, a^n, t_s \,] \tag{4.1}$$

where e is the true attitude vector containing the roll, pitch and yaw angles, p is the true position vector in north east down (NED) coordinate system [50], v^n and a^n are true velocity vectors and true acceleration vectors respectively. Lastly, t_s stands for the simulation time vector. All the vectors in true input data are discrete time vectors having a number of elements of k_s. Therefore, they can be expressed as follows:

$$e = \{e_i\}_{i=1}^{k_s} \tag{4.2}$$

$$p = \{p_i\}_{i=1}^{k_s} \quad \textbf{(4.3)}$$

$$v^n = \{v_i^n\}_{i=1}^{k_s} \quad \textbf{(4.4)}$$

$$a^n = \{a_i^n\}_{i=1}^{k_s} \quad \textbf{(4.5)}$$

$$t_s = \{t_{si}\}_{i=1}^{k_s} \quad \textbf{(4.6)}$$

4.1.1.1 Gyroscopes

As mentioned in Chapter 2.2.1, inertial sensors on a strapdown inertial navigation system, gyros and accelerometers, measure the motion of the b-frame with respect to the i-frame. Therefore, ω_{ib}^b express the data coming from the gyroscope. The superscript *b* means that the data is expressed in body axis while the subscript *ib* stands for the turn rate of the body frame with respect to the i-frame. Data coming from the three ideal orthogonal gyroscopes is expressed as in Eq. 4.7 [18].

$$\omega_{ib}^b = \omega_{nb}^b + C_n^b(\omega_{ie}^n + \omega_{en}^n) \quad \textbf{(4.7)}$$

where ω_{nb}^b is the unknown element of the equation expressing the turn rate of the body frame with respect to the navigation frame. In its long version ω_{nb}^b can be expressed as

$$\omega_{nb}^b = [\ \omega_x, \omega_y, \omega_z\ ]^T \quad \textbf{(4.8)}$$

Since ω_{nb}^b represents the turn rate of the vehicles body frame with respect to the navigation frame, it gives the attitude data of the vehicle in navigation coordinate axes.

ω_{ie}^n is the turn rate of the Earth frame with respect to the inertial frame expressed in n-frame while ω_{en}^n is the turn rate of the navigation frame with respect to the Earth frame expressed in n-frame. The turn rates ω_{ie}^n and ω_{en}^n are added to the equation in order to take the Earth rotation into consideration. Since ω_{ie}^n and ω_{en}^n are expressed in navigation frame

they are multiplied by C_n^b in order to express them in terms of body axis. For further detail regarding the direction cosine matrix reader is referred to Chapter 2.2.2.

Gyroscopes have some error types such as rate random walk noise, rate ramp noise, angle random walk noise (ARW), cross-coupling errors, biases, scale factor errors, effect of the environment factors, errors caused by axis misalignments and so on. In this simulation environment only three of them are taken into consideration which are ARW, static biases and dynamic biases since they are the most effective ones [2]. ARW is defined as a white Gaussian Noise $\eta_g = N(0, \sigma_g^2)$ [37]. On the other hand, static bias b_g is chosen randomly from the interval $[\ +b_g, -b_g\ ]$ and it is constant during the simulation [51]. However, the dynamic bias, δb_g, which is effective in low frequencies, is modeled in NaveGo as Gauss-Markov process [37], [52], whose formulation is given as

$$\eta_{g\delta b(+)} = \eta_{g\delta b} + \omega_c \tag{4.9}$$

$$\alpha = e^{-(\delta t\ o\ 1/\tau_g)} \tag{4.10}$$

$$\sigma_c^2 = {\sigma_{g\delta b}}^2\ \ o\ \ (1-\alpha^2) \tag{4.11}$$

where ω_c is a normal sequence with σ_c^2, τ_g is a correlation time, and ${\sigma_{g\delta b}}^2$ is taken approximately as the 10% of the static bias. Subscript (+) stands for the next time interval while *o* means that entry-wise matrix product. Finally, gyroscope output data with the noises is given in Eq. 4.12.

$$\omega_{noise}^b = \omega_{ib}^b + \eta_g + b_g + \eta_{g\delta b} \tag{4.11}$$

4.1.1.2 Accelerometers

First step of the accelerometer simulation starts from the true input data $T = [\ e, p, v^n, a^n, t_s\ ]$ where a^n is the acceleration data of the vehicle in navigation frame. Using the direction cosine matrix C_n^b, a^n is expressed in the body frame as in Eq. 4.12.

$$a^b = C_n^b * a^n \tag{4.12}$$

Gravity and Coriolis forces are modeled as the noises of the accelerometer in the simulation. Coriolis force is expressed as in Eq. 4.13 [18].

$$f_{cor}^{n} = S(2\omega_{ie}^{n} + \omega_{en}^{n}) \quad \textbf{(4.13)}$$

where *S* is the skew symmetric form of v^n from $T = [\, e, p, v^n, a^n, t_s \,]$. These forces can be represented in body reference frame as f^b by using the direction cosine matrix as in Eq. 4.14.

$$f^b = a^b - C_n^b(\, f_{cor}^{n} + g^n) \quad \textbf{(4.14)}$$

As for the gyroscopes, random walk noise, static noise and dynamic noise are effective in accelerometers as well. Eq. 4.15 shows the modelled output of accelerometer in simulation when considering static bias, b_f, dynamic bias, $\eta_{f\delta b}$, and the velocity random walk noise (VRW), η_f .

$$f_{noise}^{b} = f^b + \eta_f + b_f + \eta_{f\delta b} \quad \textbf{(4.15)}$$

4.2 Single and Multiple IMU SINS Comparison

True input trajectory data is used as an input for SINS whose characteristic is created in accordance with the error profile of the IMUs. Then, the output taken from SINS is fused with the GPS data and passed through the Extended Kalman Filter that is called in [37] as complementary filter. The integration of SINS, GPS and Kalman Filter is shown in Figure 4.2 where, v^n and p^n represent the velocity and position vectors coming from SINS, v_G^n and p_G^n represent the velocity and position data coming from GPS, *x* represents the state vector, $x_{(-)}$ represents the state vector belonging the previous time period, and δy and δx are used for the feedback loop. For further details regarding the algorithm the reader is referred to [2].

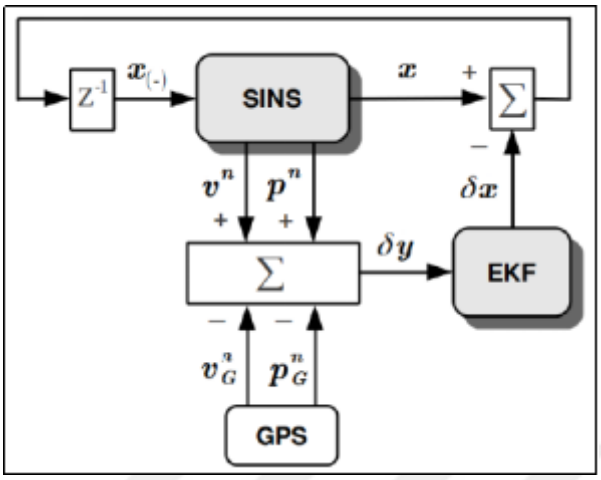


Figure 4.2 Diagram of SINS, GPS, and EKF integration [2]

Since SINS with multiple IMUs is used in this study, arithmetic mean of the three different outputs taken from Extended Kalman Filter is taken as an output of the multiple-IMU SINS. The simulation that is conducted in this study can be divided into two steps:

1. Generating the error profile of an INS employing only one IMU with no GPS aid, for three different IMUs.

2. Generating the error profile of an INS employing multiple IMUs without GPS aid.

These two steps are shown on the same graphs in Chapter 4.2.4 in order to ease the comparison.

4.2.1 Reference Trajectory Selection

Although it is possible to define different reference trajectory scenarios, the predefined trajectory reference in NaveGo simulation framework, shown in Figure 4.3, is adopted in this work as it is sufficient for the purpose of this study.

Since latitude, longitude and altitude values all change in the reference trajectory it is possible to compare the performances of the single and multiple IMU inertial navigation systems in terms mentioned variables by using the trajectory in Fig. 4.3

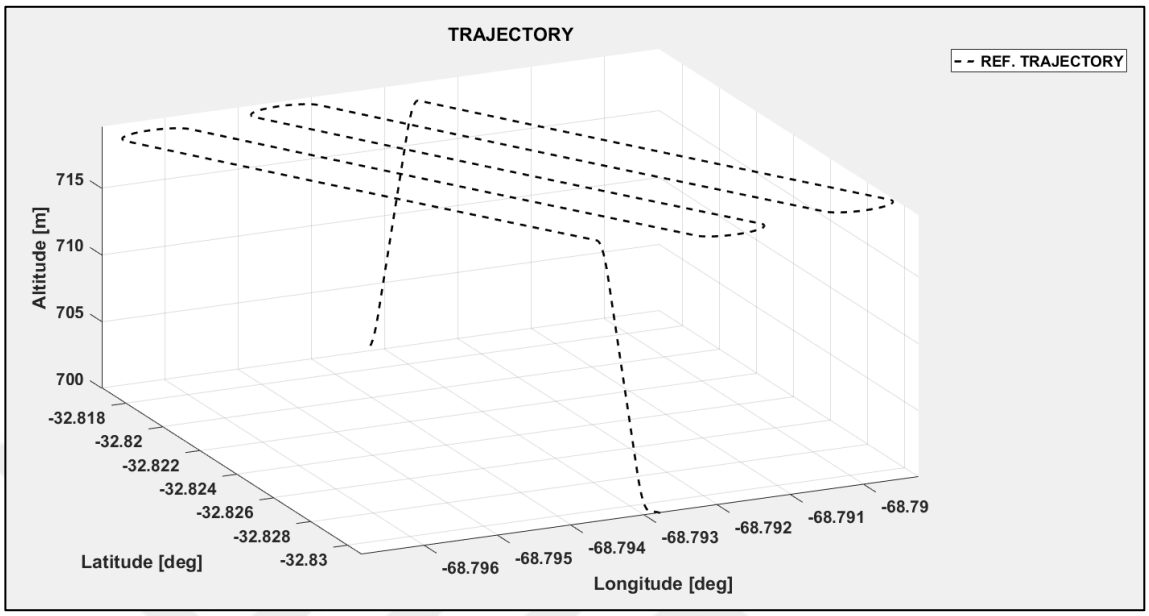


Figure 4.3 Trajectory used in this study

4.2.2 IMU Selection

IMU selection is one of the most crucial parts of this work. There are two important points regarding IMU selection. First, the error profiles of the IMUs are supposed to be similar to each other. Because, if the profiles are far away from each other, for example, one of the IMUs provides a highly errored data when the other two provide more precise data then the worst IMU corrupts the data coming from the other two IMUs. On the other hand, if the error profiles of the IMUs are close to each other then they can operate more compatible together. At one point of the navigation if one of the IMUs generates inaccurate outputs then it is most likely for the other IMUs to remedy the trajectory estimation. Therefore, the first criterion of selecting the IMUs is that their error profiles are similar to each other.

Secondly, the error profiles of the IMUs to be simulated should be formed with the help of the real IMUs. The error specifications of the real IMUs can be reached from their data sheets. By doing so, the simulation is assumed to be more realistic. Therefore, error

specifications of three different IMUs from Analog Devices are used in this work. The model number of these IMUs are namely ADIS16485, ADIS16488 and ADIS16448, which are referred as IMU1, IMU2 and IMU3 in this study respectively. The profiles of the three used IMUs mentioned above are shown in Table 4.1.

Table 4.1 IMU Profiles

	ADIS16485	**ADIS16488**	**ADIS16448**	
ARW	0.3	0.3	0.66	$deg/\sqrt{h}$
VRW	0.023	0.029	0.11	$m/s/\sqrt{h}$
***bg* (1σ)**	0.2	0.2	0.5	deg/s
***bf* (1σ)**	3	16	20	mg
Σgδb	1.7E-3	1.8E-3	4E-3	deg/s
Σfδb	0.032	0.1	0.25	mg
Frequency	128	128	128	Hz

4.2.3 GPS-denied Region Model

In order to decrease the effect of GPS on the INS, the error factor and the period of the GPS signal are increased. Hence, not only INS rarely benefits from the GPS signal due to the low frequency of the GPS, which is about 0.07 Hz, but it is also misdirected by GPS signal because of the increased error profile of GPS.

In NaveGo simulation environment, when there is a GPS aid the default reading frequency of GPS is 50 Hz. It means that at each 20 ms INS benefits from the GPS signal. On the other hand, when the frequency is decreased to 0.07 Hz to mimic a GPS-denied environment, at approximately each 15.000 ms INS is assisted by GPS data. In addition, the standard deviation constant of the position data coming from the GPS signal is also

increased approximately 20 times for the simulation of GPS-denied environment. Therefore, the errored GPS data become more probable to misguide the INS.

4.2.4 Simulation Results

As mentioned in *Simulation Method* section, the simulation results for different situations are shown on the same graph for the sake of easy comparison. When the effect of the GPS signal on INS is decreased by the method explained in *Simulation of GPS-Denied Environment* section, the error profiles from Figure 4.5, Figure 4.6 and Figure 4.7 are obtained for latitude, longitude and altitude errors respectively. Altitude specifies the elevation of the vehicle above sea level while latitude and longitude are illustrated in Figure 4.4 [18].

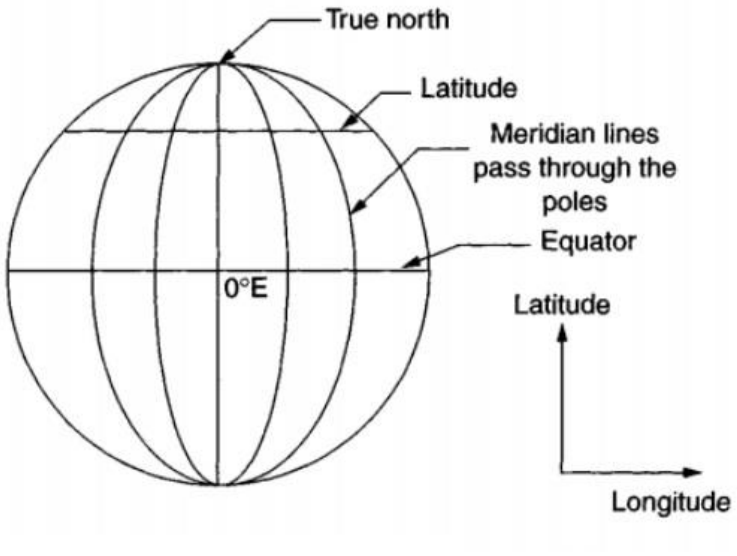


Figure 4.4 Geographic coordinate system [18]

As mentioned in *IMU Selection* section, IMU1, IMU2 and IMU3 denote ADIS16485, ADIS16488 and ADIS16448 respectively. Therefore, on the legends of the following graphs *IMU1* stands for *INS aided with IMU1 data*, *IMU2* denotes *INS aided with IMU2 data* and *IMU3* stands for *INS aided with IMU3 data.* On the other hand, *IMU1+IMU2+IMU3* denotes *INS aided with Multiple IMUs.* MEMS-IMUs can be

affected by many different environmental factors. Hence, the simulations depending on only one IMU may result in a highly errored outcome. On the other hand, using multiple IMUs may be helpful to fix the error profile due to the fact that if one of the IMUs gives a wrong data at one point, it is probable that the others give a correct data at the same point. It is possible to see this positive effect of multiple-IMU system in the followings graphs.

In Figure 4.5, the latitude error of the system with IMU3 gives a highly errored outcome which is approximately 550 meters at 300th second. However, at that point since the data coming from the other IMUs are relatively correct, INS aided with multiple IMUs -that is shown in red- results in a more acceptable error profile which is approximately 100 meters. It means that multiple IMU system configuration provides us with an 82% reduction of latitude error.

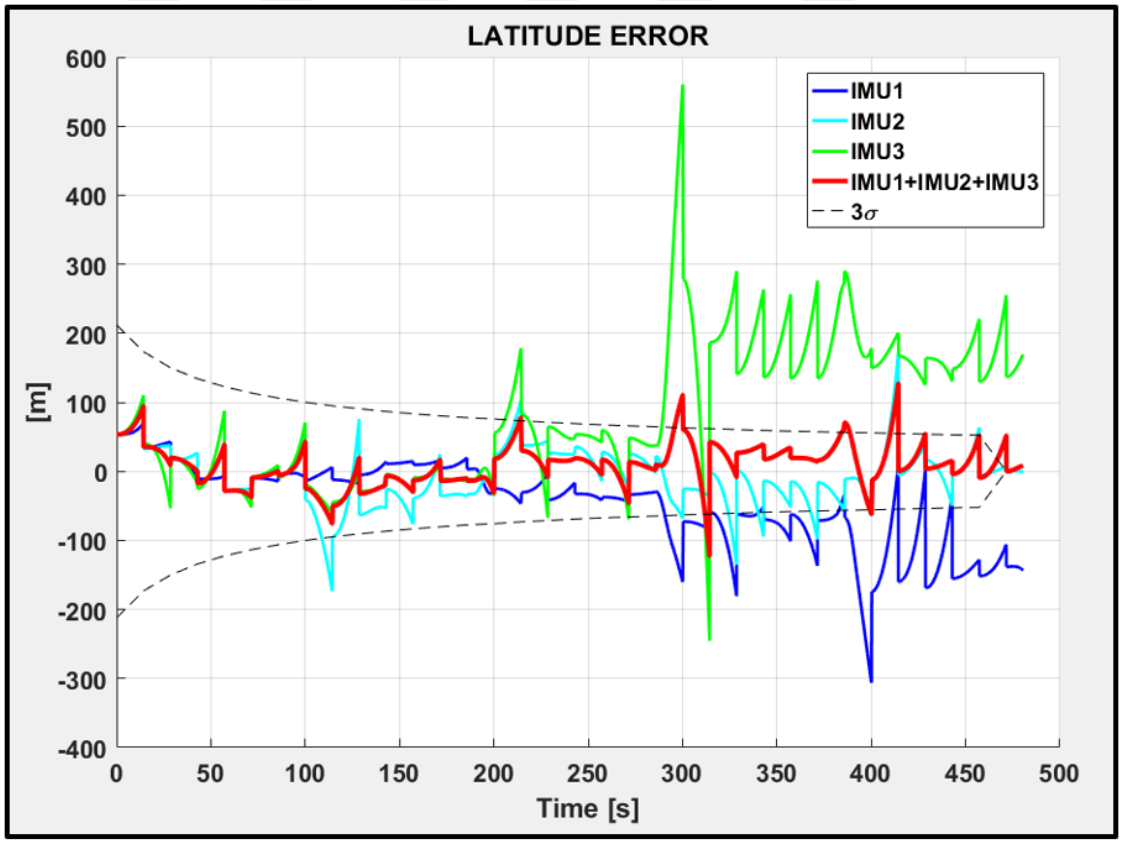


Figure 4.5 Latitude errors of the INSs without GPS aid

In Figure 4.6, the longitude error of the INS with IMU1 fails at 410th second with a highly errored data of approximately 270 meters. However, at that point thanks to the correct data coming from the other IMUs, multiple IMU system results in a much better longitude error profile which is approximately 80 meters. It means that INS with multiple IMUs provide us with 85% improvement on longitude error.

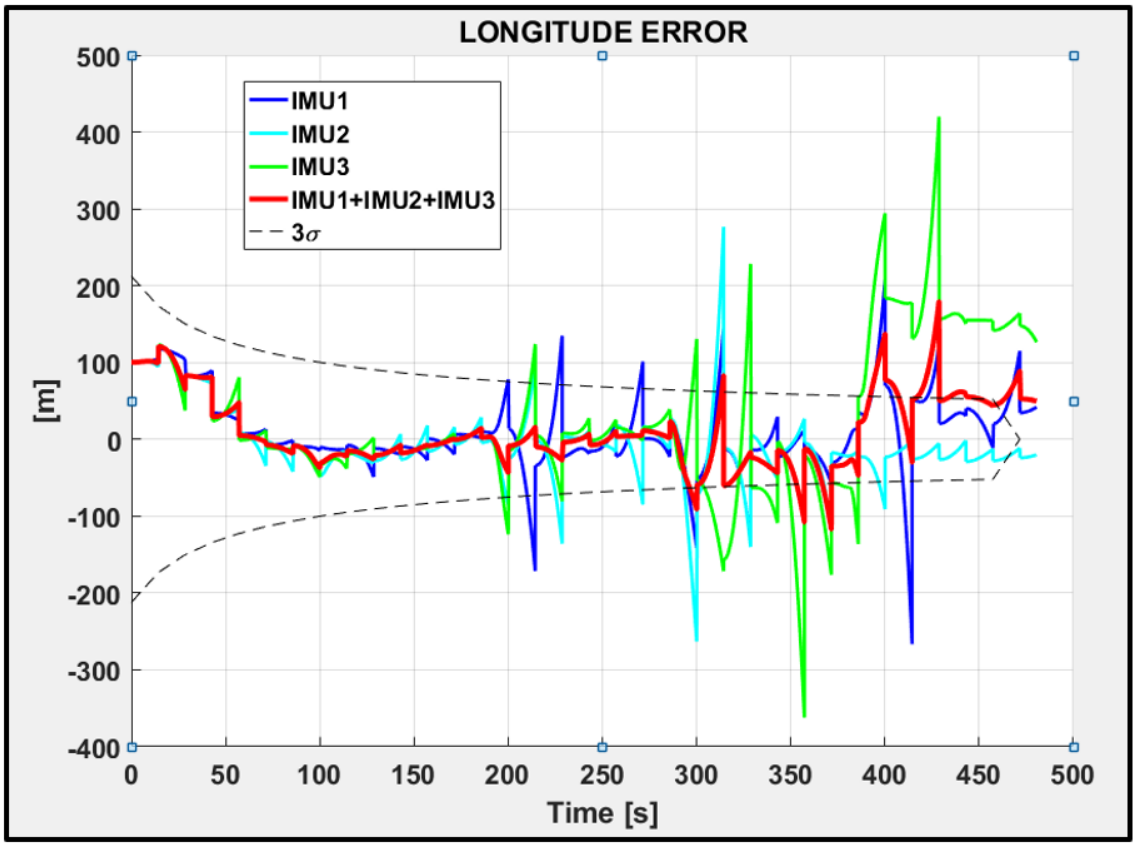


Figure 4.6 Longitude errors of the INSs without GPS aid

The altitude error of the INS with IMU3 results in an errored data of about 230 meter around 370th second as seen in Figure 4.7. On the other hand, with the help of the other IMUs, INS with multiple IMUs - shown in red – results in a much better error profile which is approximately 40 meters. It means that INS with multiple IMUs achieves nearly 83% decrease in altitude error.

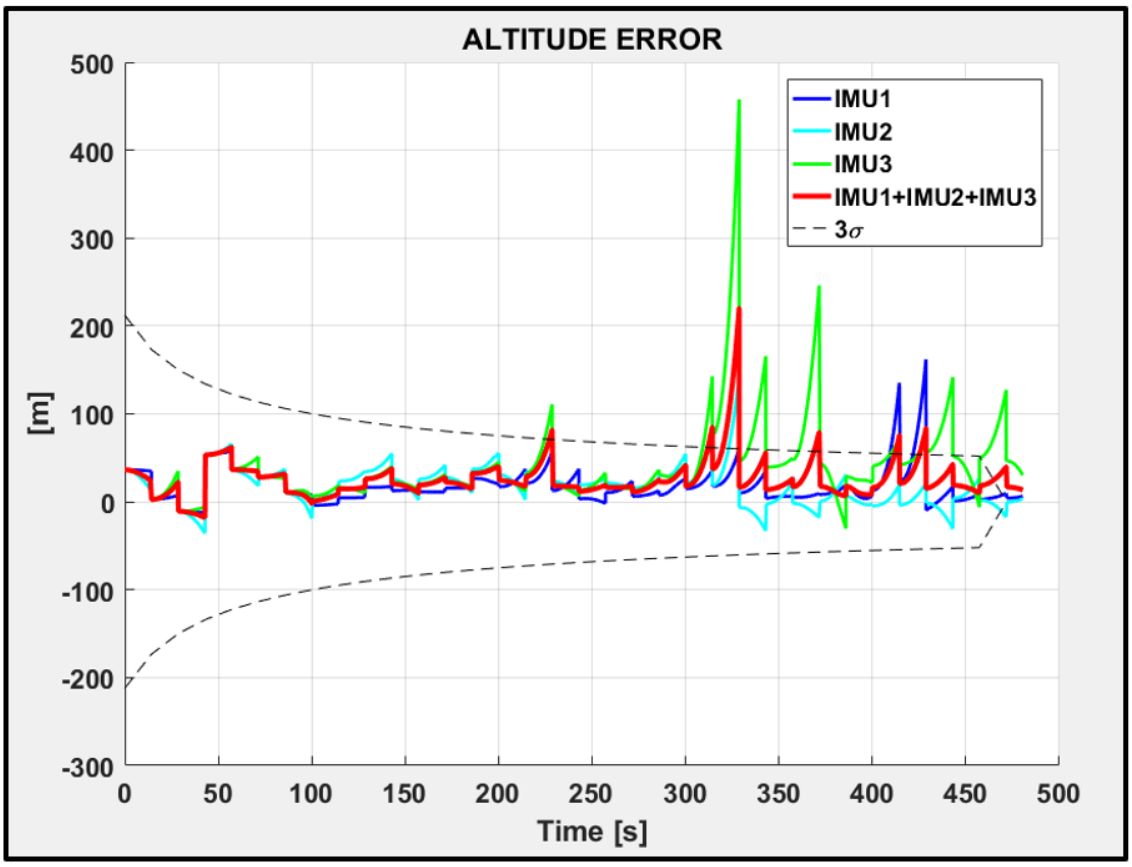


Figure 4.7 Altitude errors of the INSs without GPS aid

CHAPTER 4

CONCLUSIONS, PERSPECTIVES AND FUTURE WORKS

In this thesis, a method is suggested to fix the error profile of an INS system in a GPS-denied environment using NaveGo simulation framework. The suggested method is utilizing multiple IMUs in an INS which is not aided by a GPS signal. Proposed method is demonstrated by comparing the error profile of an *INS with a single IMU* and an *INS with a cluster of three IMUs*. According to the simulation results, the system aided by multiple IMUs results in a better error profile in comparison with the INS which utilizes only one IMU.

Unique side of this study in comparison with the similar researches conducted on the same topic is that data coming from different IMUs having different error profiles are used for the navigation in GPS-denied region. For example, in [11] and [12] same type of inertial measurement units is used for the multiple IMU navigation system as stated in Chapter 3.3. However, in this thesis, different type of real IMU profiles are used which are namely ADIS16485, ADIS16488 and ADIS16448.

Another important point is that mentioned IMUs can be easily obtained in real life with a low price. It is claimed that at one point of the navigation if one of the IMUs generates inaccurate outputs then it is most likely for the other IMUs to remedy the trajectory estimation. This assertion is supported by the simulation results that is discussed in Chapter 4.2.4. Thus, this study draws attention to a method worthy of study to obtain more accurate results from a navigation system designed using simple IMUs that are easily accessible.

No matter how comprehensive a simulation environment is designed, it cannot always accurately reflect the real environment. Therefore, the results obtained in the simulation environment should be a pioneer of real applications. In order to carry the study in this

thesis to a higher level, it is aimed to test the proposed method on an unmanned aerial vehicle. After the field test, it can be determined how much the real test results comply with the simulation results. Furthermore, it is planned to repeat the simulation tests and the actual field tests by increasing the number of IMUs used.

REFERENCES

[1] Maenaka, K. MEMS inertial sensors and their applications. 5th International Conference on Networked Sensing Systems. Retrieved May 20, 2019, from https://ieeexplore.ieee.org/abstract/document/4610859. August 29, 2008.

[2] Gonzalez, R., Giribet, J. I., & Patino, H. D. NaveGo: a simulation framework for low-cost integrated navigation systems. CEAI, 17 (2), 110-120. 2015.

[3] Guerrier, S. Improving accuracy with multiple sensors: study of redundant MEMS-IMU/GPS configurations. Proceedings of the 22nd International Technical Meeting of the Satellite Division of the Institute of Navigation, 3114-3121. 2009.

[4] Waegli, A., Guerrier, S., & Skaloud, J. Redundant MEMS-IMU integrated with GPS for performance assessment in sports. IEEE/ION Position, Location and Navigation Symposium. Retrieved May 21, 2019, from https://ieeexplore.ieee.org/document/4570079 2008. September 3, 2008.

[5] Hardy, J., Strader, J., Gross, J. N., Gu, Y., Keck, M., Douglas, J., et.al. Unmanned aerial vehicle relative navigation in GPS-denied environments. IEEE/ION Position, Location and Navigation Symposium (PLANS). Retrieved May 22, 2019, from https://ieeexplore.ieee.org/document/7479719. May 30, 2016.

[6] Tsai, S., & Zhuang, S. Optical flow sensor integrated navigation system for quadrotor in GPS-denied environment. International Conference on Robotics and Automation Engineering (ICRAE). Retrieved May 25, 2019, from https://ieeexplore.ieee.org/document/7738795. November 10, 2016.

[7] Bancroft, J. B., & Lachapelle, G. Data fusion algorithms for multiple inertial measurement units. Sensors, 11 (7), 6771-6798. Retrieved May 30, 2019, from https://www.ncbi.nlm.nih.gov/pmc/articles/PMC3231672/. June 29, 2011.

[8] Bayard, D. S., & Ploen, S. R. High accuracy inertial sensors from inexpensive components. U.S. Patent Documents. Patent No: 6,882,964 B2. April 19, 2005.

[9] Chang, H., Xue, L., Qin, W., Yuan, G., & Yuan, W. An integrated MEMS gyroscope array with higher accuracy output. Sensors, 8 (4), 2886-2899. Retrieved May 10, 2019, from https://www.ncbi.nlm.nih.gov/pubmed/27879855. April 28, 2008.

[10] Tanenhaus, M., Carhoun, D., Geis, T., Wan, E., & Holland, A. Miniature IMU/INS with optimally fused low drift MEMS gyro and accelerometers for applications in GPS-denied environments. IEEE/ION Position Location and Navigation Symposium (PLANS), 259-264. Retrieved May 5, 2019, from https://ieeexplore.ieee.org/document/6236890. July 12, 2012.

[11] Skog, I., Nilsson, J. O., & Handel, P. An open-source multi inertial measurement unit (MIMU) platform. International Symposium on Inertial Sensors and Systems (ISISS). Retrieved March 30, 2019, from https://ieeexplore.ieee.org/document/6782523. April 3, 2014.

[12] Shahri, A. M., & Rasoulzadeh, R. Implementation of a low- cost multi-IMU by using information form of a steady state Kalman Filter. AUT Journal of Electrical Engineering, 49 (2), 195-204. Retrieved March 17, 2019, from https://eej.aut.ac.ir/article_1972.html. September 17, 2017.

[13] Retrieved May 17, 2019, from https://www.direnc.net/l3g4200d-gyroscope-sensor.

[14] Noureldin, A., Karamat, T. B., & Georgy, J. Fundamentals of inertial navigation, satellite-based positioning and their integration. Springer-Verlag Berlin Heidelberg. 2013.

[15] Weems, W. R. An Introduction to the study of gyroscopic instruments. MIT Department of Aeronautical Engineering, Cambridge. 1948.

[16] Chatfield, A. B. Fundamentals of high accuracy inertial navigation (Volume 174). American Institute of Aeronautics and Astronautics. 1997.

[17] Foucault, L. Sur les phénomènes d'orientation des corps tournants entraînés par un axe fixe à la surface de la terre — Nouveaux signes sensibles du mouvement diurne. Compt. Rend., 35, 424–427. 1852.

[18] Titterton, D. H., & Weston J. L. Strapdown inertial navigation technology (2nd Ed.). Institution of Engineering and Technology, USA. 2004.

[19] Sagnac, M. G. Léther lumineux démontré par leffet du vent relative d'éther dans un interféromètre en rotation uniforme. Compt. Rend., 157, 708-710. 1914.

[20] Kelly, A. G. The Sagnac Effect and the GPS synchronization of clock-stations. Institution of Engineers of Ireland. 1995.

[21] Ghatak, A., & Thyagarajan, K. Introduction to fiber optics. Cambridge University Press. 1998.

[22] Burns, W. K. Optical fibers rotation sensing. Academic Press, Boston. 1994.

[23] Park, S., Horowitz, R., & Tan, C. W. Dynamics and control of a MEMS angle measuring gyroscope. Sensors and Actuators, 144 (1), 56-63. Retrieved March 30, 2019, from https://www.sciencedirect.com/science/article/pii/S0924424708000101. May 28, 2008.

[24] Augustyn, A., Bauer, P., Duignan, B., Eldridge, A., Gregersen E., McKenna, A., et al. Coriolis Force. Encyclopedia Britannica. Retrieved May 5, 2019, from https://www.britannica.com/science/Coriolis-force. July 20, 1998.

[25] Passaro, V. M. N., Cuccovillo, A., Vaiani, L., De Carlo, M., & Campanella, C. E. Gyroscope technology and applications: a review in the industrial perspective. Sensors (17) 10. Retrieved March 13, 2019, from https://www.ncbi.nlm.nih.gov/pmc/articles/PMC5677445/. October 7, 2017.

[26] Xie, H., & Fedder, G. K. Integrated microelectromechanical gyroscopes. Journal of Aerospace Engineering 16 (2), 65–75. April 1, 2003.

[27] Jiang, X., Seeger, J. I., Kraft, M., & Boser, B. E. A monolithic surface micromachined z-axis gyroscope with digital output. Digest of Technical Papers, Symposium on VLSI Circuits, Honolulu, 16–19. Retrieved March 15, 2019, from https://ieeexplore.ieee.org/document/852839. August 6, 2002.

[28] Tinder, R. F. Relativistic flight mechanics and space travel: a primer for students, engineers and scientists (synthesis lectures on engineering series). Morgan & Claypool Publishers. 2007.

[29] Taylor, E. F., & Wheeler, J. A. Spacetime Physics (1st Ed.). W.H. Freeman, San Francisco. 1966.

[30] Zukauskas, W. Fiber optic accelerometer investigation. Master Thesis, Massachusetts Institute of Technology. 1987.

[31] Beeby, S., Ensell, G., Kraft, M., & White, N. MEMS mechanical sensors. Artech House, London. 2004.

[32] Lyshevski, S. E. MEMS and NEMS: systems, devices and structures. CRC Press LLC, USA. 2002.

[33] Andrejašic, M. Mems accelerometers. Retrieved May 3, 2019, from http://mafija.fmf.uni-lj.si/seminar/files/2007_2008/MEMS_accelerometers-koncna.pdf. March 1, 2008.

[34] Leondes, C. T. (Ed.). MEMS/NEMS handbook techniques and applications, volume 4: sensors and actuators. Springer, USA. 2006.

[35] Bekir, E. Introduction to modern navigation systems. World Scientific Publishing. 2007.

[36] Britting, K. Inertial navigation system analysis. Wiley Interscience, New York. 1971.

[37] Farrell, J. A. Aided navigation GPS with high rate sensors. Mcgraw-Hill. 2008.

[38] Whyte, H. D., & Bailey, T. Simultaneous localisation and mapping: part I the essential algorithms. IEEE Robotics & Automation Magazine, 13 (2), 99-110. Retrieved May 8, 2019, from https://ieeexplore.ieee.org/document/1638022. June 5, 2006.

[39] Balamurugan, G., Valarmathi, J., & Naidu, V. Survey on UAV navigation in GPS-denied environments. International conference on Signal Processing, Communication, Power and Embedded System (SCOPES). Retrieved March 21, 2019, from https://ieeexplore.ieee.org/document/7955787. June 26, 2017.

[40] Thrun, S., Beetz, M., Bennewitz, M., Burgard, W., Cremers, A., Dellaert, F., et. al. Probabilistic algorithms and the interactive museum tour-guide robot Minerva. The International Journal of Robotics Research, 19 (11), 972-999. Retrieved May 11, 2019, from https://journals.sagepub.com/doi/10.1177/02783640022067922. November 1, 2000.

[41] Thrun, S. Finding landmarks for mobile robot navigation. IEEE International Conference on Robotics and Automation (ICRA). Retrieved May 7, 2019, from https://ieeexplore.ieee.org/document/677210. August 6, 2002.

[42] Frintrop, S., Jensfelt, P., & Christensen, H. Attentional landmark selection for visual SLAM. IEEE/RSJ International Conference on Intelligent Robots and Systems. Retrieved March 16, 2019, from https://ieeexplore.ieee.org/document/4058779. January 15, 2007.

[43] Kropatsch, W. G., Sablatnig, R., Hanbury, A. (Ed.). Pattern Recognition (117-124). Springer-Verlag Berlin Heidelberg. 2005.

[44] Tsotsos, J. K., Culhane, S. M., Wai, W. Y. K., Lai, Y., Davis, N., & Nuflo, F. Modeling visual attention via selective tuning. Artificial Intelligence, 78 (1-2), 507–545. Retrieved March 8, 2019, from https://www.sciencedirect.com/science/article/pii/0004370295000259. October 1, 1995.

[45] Itti, L., Koch, C., & Niebur, E. A model of saliency-based visual attention for rapid scene analysis. IEEE Transactions on Pattern Analysis and Machine Intelligence, 20 (11), 1254–1259. Retrieved March 9, 2019, from https://ieeexplore.ieee.org/document/730558. November 1, 1998.

[46] Nister, D., Naroditsky, O., & Bergen, J. Visual odometry. IEEE Computer Society Conference on Computer Vision and Pattern Recognition, 652–659. Retrieved May 15, 2019, from https://ieeexplore.ieee.org/document/1315094. July 19, 2004.

[47] Scaramuzza, D., & Fraundorfer, F. Visual Odometry Tutorial. IEEE Robotics and Automation Magazine, 18 (4), 80-92. Retrieved May 14, 2019, from https://ieeexplore.ieee.org/document/6096039. December 8, 2011.

[48] Zhang, J., & Singh, S. LOAM: Lidar odometry and mapping in real-time. Robotics: Science and Systems Conference. Retrieved from March 8, 2019, from https://www.semanticscholar.org/paper/LOAM%3A-Lidar-Odometry-and-Mapping-in-Real-time-Zhang-Singh/719fd645c4da6575ab0e774891ba30d7dfcc53aa. July 12, 2014.

[49] Zhang, J., & Singh, S. Laser-visual-inertial odometry and mapping with high robustness and low drift. Journal of Field Robotics. 35, 1242-1264. Retrieved May 16, 2019, from https://onlinelibrary.wiley.com/doi/epdf/10.1002/rob.21809. July 9, 2018.

[50] Cai, G., Chen, B.M., & Lee, T.H. Unmanned rotorcraft systems. Springer London, UK. 2011.

[51] Groves, P. D. Principles of GNSS, Inertial, and Multisensor Integrated Navigation Systems. Artech House, USA. 2008.

[52] Strus, J. M., Kirkpatrick, M., & Sinko J. W. Development of a high accuracy pointing system for maneuvering platforms. 20th International Technical Meeting of the Satellite Division of The Institute of Navigation, 2541-2549. Retrieved April 22, 2019, from https://www.ion.org/publications/abstract.cfm?articleID=7518. September 25, 2007.

[53] Photo taken by Stephane Magnenat at the National Conservatory of Arts and Crafts Museum, Paris. Retrieved May 1, 2019, from https://en.wikipedia.org/wiki/Gyroscope#/media/File:Foucault's_gyroscope.jpg. June 24, 2008.

[54] Retrieved May 10, 2019, from https://www.grc.nasa.gov/www/k-12/airplane/rotations.html

[55] El-Sheimy, N., Hou, H., & Niu, X. Analysis and modeling of inertial sensors using Allan variance. IEEE Transactions on Instrumentation and Measurement, 57 (1), 140-149. Retrieved April 30, 2019, from https://ieeexplore.ieee.org/document/4404126. December 17, 2007.

[56] Retrieved May 17, 2019, from https://www.direnc.net/9-eksenli-imu-sensoru-gyro-yukseklik-ivme-hiz?lang=tr&h=8b97dadd&gclid=CjwKCAjwlPTmBRBoEiwAHqpvhZnklvS1GSt1p_ZjO1NJLo36d1yc45Yb9XKJwX-Jbz9fs_itPImBExoCkWoQAvD_BwE.

CURRICULUM VITAE

PERSONAL INFORMATION



Name Surname: Osman TOKLUOĞLU

Date of Birth: 13.08.1992

Phone: (530) 923 1293

E-Mail: osmantokluoglu92[at]gmail.com
otokluoglu[at]ybu.edu.tr

EDUCATION

High School: Gazi Anadolu Lisesi

Bachelor: Middle East Technical University**,** Electrical & Electronics Engineering

WORK EXPERIENCE

Research Assistant at AYBU Electrical & Electronics Engineering Department since 2018.

TOPIC OF INTEREST

THz System Design, FPGA Design, Verilog HDL, Telecommunication, Inertial Navigation System (INS), Defense Industry Applications